A new operator-splitting finite element scheme for reactive transport modeling in saturated porous media

Renchao Lu[a], Thomas Nagel[b,c], Jenna Poonoosamy[d], Dmitri Naumov[b], Thomas Fischer[a], Vanessa Montoya[a], Olaf Kolditz[a,c,e] and Haibing Shao[a,*]

[a]Helmholtz Centre for Environmental Research - UFZ, Leipzig, Germany
[b]Technische Universität Bergakademie Freiberg, Freiberg, Germany
[c]TUBAF-UFZ Centre for Environmental Geosciences, Germany
[d]Institute of Energy and Climate Research (IEK-6): Nuclear Waste Management and Reactor Safety, Forschungszentrum Jülich GmbH, 52425 Jülich, Germany
[e]Technische Universität Dresden, Dresden, Germany

ARTICLE INFO

Keywords:
Reactive transport modeling
Operator splitting approach
Integration-point collocation scheme

ABSTRACT

The operator splitting approach has been widely accepted since it was introduced as a means to solve reactive transport problems. The conventional operator-splitting finite element scheme (Nodal-OS) handles speciation calculations on nodes, resulting in a mixing of heterogeneous reactions on opposing sides in multi-layer systems. Such mixing, however, is not physically accurate. In this context, we propose a new operator-splitting finite element scheme (IP-OS) for reactive transport modeling in saturated porous media. In contrast to the conventional scheme, speciation calculations are performed on integration points rather than on nodes in the new scheme. The implementation of the IP-OS scheme is verified through comparison with an analytical solution of a coupled diffusion-dissolution problem. On this basis, two representative benchmarks are used to examine the advantages and disadvantages of IP-OS. IP-OS is found to have the following advantages and disadvantages compared to Nodal-OS: (1) IP-OS is more accurate; (2) IP-OS is more straightforward to implement; (3) IP-OS is less sensitive to grid resolution and is numerically more stable with coarser grid spacing; and (4) IP-OS is computationally more expensive. In light of the above pros and cons, we recommend using Nodal-OS in cases where chemical reactions do not affect transport properties, and IP-OS in multi-layer heterogeneous cases where chemical reactions alter transport properties of porous media.

1. Introduction

The development of continuum-scale reactive transport models dates back to the early 1980's when Lichtner (1985) outlined the theoretical framework for reactive transport modeling (Steefel et al., 2005). Over the past decades, many renowned reactive transport modeling software packages have emerged (Steefel et al., 2015; Steefel, 2019), such as COMSOL-Phreeqc (Wissmeier and Barry, 2011; Nardi et al., 2014; Guo et al., 2018), COMSOL-GEM (Azad et al., 2016), CORE^{2D} (Samper et al., 2000), CrunchFlow (Steefel, 2009), CSMP++GEM (Yapparova et al., 2017), DuCOM-Phreeqc (Elakneswaran and Ishida, 2014), FEniCS-Reaktoro (Damiani et al., 2020), Frachem (Bächler and Kohl, 2005), HP1/HPx (Jacques and Šimůnek, 2005), MATLAB-Phreeqc (Muniruzzaman and Rolle, 2016), MIN3P (Mayer and MacQuarrie, 2010), OpenGeoSys-5#GEM (Kosakowski and Watanabe, 2014; Poonoosamy et al., 2018), OpenGeoSys-5#Phreeqc (He et al., 2015), ORCHESTRA (Meeussen, 2003), Proost (Gamazo et al., 2016), ReactMiCP (Georget et al., 2017), and ToughReact (Xu et al., 2006, 2011). With extensive benchmark testing conducted in recent years, these software packages have become more robust and reliable (Druhan and Tournassat, 2019; Molins and Knabner, 2019), and are used in a variety of subsurface applications, e.g., nuclear waste disposal (Kosakowski and Berner, 2013; Berner et al., 2013; Shao et al., 2013; Gin et al., 2013; Kosakowski et al., 2014; Huang et al., 2018; Idiart et al., 2020), geothermal energy systems (Yapparova et al., 2019; Fumagalli and Scotti, 2021), hydrocarbon reservoir production (Ballarini et al., 2014), groundwater management (Rodríguez-Escales et al., 2020), waste-rock weathering (Seigneur

*Corresponding author at: Helmholtz Centre for Environmental Research - UFZ, Leipzig, Germany.
E-mail address: haibing.shao@ufz.de (H. Shao).
ORCID(s): 0000-0002-5762-3036 (R. Lu); 0000-0001-8459-4616 (T. Nagel); 0000-0003-0090-1522 (J. Poonoosamy); 0000-0001-6680-1028 (D. Naumov); 0000-0002-4751-3597 (V. Montoya); 0000-0002-8098-4905 (O. Kolditz); 0000-0002-9214-8349 (H. Shao)

et al., 2020), energy storage (Bonte et al., 2014; Nagel et al., 2016), waste treatment (Boog et al., 2019, 2020; Chen et al., 2020), mine waste deposits (Bea et al., 2010) and/or CO_2 sequestration (Pruess et al., 2004; Beyer et al., 2012; Li et al., 2014).

Essentially, all the aforementioned software packages solve a set of partial differential equations consisting of the fluid flow and reactive transport equations. The majority of software packages adopt the finite element, finite volume, and/or finite difference methods for numerical approximation of equation systems. The pros and cons of different numerical methods for solving reactive transport problems have been extensively discussed in Våg et al. (1996); Lichtner (1996); Chen and Ewing (1997); Wang (1998); Wang et al. (1999); Cirpka et al. (1999); Ewing et al. (2000); Ewing and Wang (2001); Kanney et al. (2003); Sahimi (2011); Miller et al. (2013). After the space-time discretization of the governing equations is performed using either of the above numerical methods, there are two possible numerical solution strategies for solving the fully discretized reactive transport equation: (1) the global implicit approach (Kräutle and Knabner, 2007; Hoffmann et al., 2010; Carrayrou et al., 2010; Brunner and Knabner, 2019), and (2) the operator splitting approach (OS) (Chiang et al., 1991; Valocchi and Malmstead, 1992; Barry et al., 1996; Saaltink et al., 2001; Bell and Binning, 2004; Geiser, 2011). The global implicit approach aims to solve the discretized reactive transport equation in one step. One may call a specified chemical solver, e.g., Phreeqc (Parkhurst and Appelo, 2013), GEM (Kulik et al., 2013), and Reaktoro (Leal et al., 2017), in each iteration step to solve a particular set of mass/energy balance equations underlying the heterogeneous reaction term. Compared to OS, the global implicit approach yields a more accurate numerical solution, but it requires more iterations to reach a solution. The majority of the computational time is spent in the iterative computation due to the strong coupling between the transport and reaction processes. Instead, OS treats the reactive transport process as a two-stage process — the transport process is followed by the reaction process over a time step. First, one solves the discretized dispersion-advection equation, and then the discretized reaction equation using the solution of the transport stage as the initial solution. In solving the reaction equation, speciation calculations can be outsourced to an external chemical solver, regardless of which numerical solution strategy is employed. As the degree of nonlinearity of the reactive transport equation is reduced by solving the linear advection-dispersion equation and the nonlinear reaction equation sequentially, it is easier to reach convergent solutions at the expense of numerical accuracy. In order to limit the loss of numerical accuracy to an acceptable level, mesh refinement and a reduced time step size are typically implemented. The numerical accuracy and convergence rate of each approach together with different linearization schemes (Newton's method, trust region Newton method, modified Picard method, and L-scheme, c.f., Illiano et al. (2021)) have been extensively discussed in Yeh and Tripathi (1989); Celia et al. (1990); Walter et al. (1994); Barry et al. (1996); Saaltink et al. (2000); Carrayrou et al. (2004); Molins et al. (2004); Jacques et al. (2006); Fahs et al. (2008); Estep et al. (2008); Samper et al. (2009); Wang and Tchelepi (2013); List and Radu (2016); Mitra and Pop (2019).

To the authors' knowledge, however, the long-established operator-splitting finite element scheme (OS-FE) does not work as described above. It is typical to begin with OS, then move on to the space-time discretization of the transport equation and reaction equation. As an ordinary differential equation, the reaction equation does not contain any spatial derivative terms. Therefore, it is not deemed necessary for the equation to be discretized using the finite element method, as it is for the transport equation. Rather, the solution of the reaction equation throughout the domain is simply executed on the nodes of the existing discretization of the transport process. Consequently, speciation calculations are performed on the nodes. This conventional scheme (referred to as Nodal-OS hereafter) takes full advantage of the flexibility in choice of numerical techniques that comes with OS. On the other hand, the collocation schemes employed in the space discretization of the transport equation and reaction equation are entirely different from one another. In the transport equation, integration points are chosen as collocation points, while in the reaction equation, nodes are selected as collocation points. When considering the geochemical interactions at mineral interfaces, this inconsistency will lead to a mixing of heterogeneous reactions on opposing sides of the interface. In addition, it is difficult to implement Nodal-OS algorithmically since every time step requires repeated extrapolation and interpolation between integration points and nodes in order to perform speciation calculations on nodes.

In this work, we present a new operator-splitting finite element scheme for reactive transport modeling in saturated porous media (IP-OS). In IP-OS, the transport equation and reaction equation are spatially discretized using a uniform collocation scheme. Specifically, Gaussian integration points are used as collocation points. Our approach is to first revisit the governing equations for reactive transport processes, and then formulate the IP-OS scheme (see Section 2). The new scheme is then implemented in the open source simulator OpenGeoSys-6 (Kolditz et al., 2012; Bilke et al., 2019), where the chemical solver Phreeqc (Parkhurst and Appelo, 2013) is also integrated for speciation calculations (OpenGeoSys-6#Phreeqc). The implementation is verified against an analytical solution of a coupled

diffusion-dissolution problem (see Appendix A). In Section 3, we examine two benchmarks to identify the advantages and disadvantages of IP-OS in comparison with Nodal-OS. In the following section, we then measure the computational performance of Nodal- and IP-OS in 1D and 3D settings, and then provide a comparison of these two OS-FE schemes from the perspective of implementation. Finally, we conclude with a recommendation regarding the circumstances in which IP-OS or Nodal-OS may be more suitable.

2. Theory

2.1. Fluid flow

Following the principle of mass conservation, the continuity equation for flowing fluid in a saturated porous medium is as follows:

$$\frac{\partial \phi}{\partial t} + \frac{\phi}{\rho^{\mathrm{l}}}\frac{\partial \rho^{\mathrm{l}}}{\partial p}\frac{\partial p}{\partial t} + \nabla \cdot \mathbf{q} + Q_p = 0, \tag{1}$$

where ϕ [-] is the porosity, t [s] is the time, ρ^{l} [kg/m^3] is the fluid density, p [Pa] is the hydraulic pressure, $\mathbf{q}$ [m/s] is the Darcy flux with laminar flow assumptions, and Q_p [1/s] is the source-sink term. According to Darcy's Law, the flux $\mathbf{q}$ is related to the pressure drop and body forces through

$$\mathbf{q} = -\frac{\mathbf{k}}{\mu}\left(\nabla p - \rho^{\mathrm{l}}\mathbf{g}\right), \tag{2}$$

where $\mathbf{k}$ [m^2] is the intrinsic permeability, μ [Pa·s] is the fluid dynamic viscosity, and $\mathbf{g}$ [m/s^2] is the gravity vector.

Given the water-rock interaction, the rate of change in porosity is affected not only by pressure, but also by reaction kinetics, which can be described as follows:

$$\frac{\partial \phi}{\partial t} = \frac{\partial \phi}{\partial p}\frac{\partial p}{\partial t} + \sum_{m=1}^{N_m} A_m r_m V_{\mathrm{m},m}, \tag{3}$$

where A_m [m^2/m^3] is the reactive surface area of a solid constituent (relative to the representative elementary volume), r_m [mol/m^2/s] is its dissolution or precipitation rate, and $V_{\mathrm{m},m}$ [m^3/mol] is its molar volume.

Upon insertion of Equation (3) back into Equation (1), the mass continuity equation is expressed in terms of hydraulic pressure as follows:

$$S_{\mathrm{s}}\frac{\partial p}{\partial t} + \nabla \cdot \mathbf{q} + Q_p + \cancel{\sum_{m=1}^{N_m} A_m r_m V_{\mathrm{m},m}} = 0, \tag{4}$$

where S_{s} [1/Pa] is the specific storage, i.e., $S_{\mathrm{s}} = \frac{\partial \phi}{\partial p} + \frac{\phi}{\rho^{\mathrm{l}}}\frac{\partial \rho^{\mathrm{l}}}{\partial p}$. Geochemical reactions typically occur at very low rates, so the final term on the left side of the equation is usually ignored. As a result, geochemical reactions primarily affect fluid flow through altered intrinsic permeability.

2.2. Reactive mass transport

In saturated porous media, reactive transport processes can be described by the advection-dispersion-reaction equation as follows: (Kirkner and Reeves, 1988; Steefel and Lasaga, 1994; Yuan et al., 2016)

$$\frac{\partial\left(\phi c_{T\alpha}\right)}{\partial t} + \nabla \cdot \left(\mathbf{q}c_{T\alpha} - \phi \mathbf{D}\nabla c_{T\alpha}\right) + R_{\alpha}^{\min} = 0, \quad \alpha = 1, .., N_p, \tag{5}$$

where $c_{T\alpha}$ [mol/m^3] is the total concentration of the primary species α, $\mathbf{D}$ [m^2/s] is the hydrodynamic dispersion tensor, and $R_{\alpha}^{\min}$ [mol/m^3/s] is the heterogeneous reaction term.

The total concentration of the primary species α is defined as (Reed, 1982; Lichtner, 1985)

$$c_{T\alpha} = c_{p\alpha} + \sum_{\beta=1}^{N_s} \upsilon_{\beta\alpha} c_{s\beta}, \quad \alpha = 1, .., N_p, \tag{6}$$

where $c_{p\alpha}$, $c_{s\beta}$ [mol/m^3] are the molar concentration of the primary species α and secondary species β, and $\upsilon_{\beta\alpha}$ is the stoichiometric coefficient of the primary species α in a reversible aqueous reaction of the form

$$A_\beta \rightleftharpoons \sum_{\alpha=1}^{N_p} \upsilon_{\beta\alpha} A_\alpha, \quad \beta = 1, .., N_s, \tag{7}$$

where A_α, A_β are the chemical formulas of the primary species α and secondary species β.

The hydrodynamic dispersion tensor $\mathbf{D}$ is given as (Scheidegger, 1961)

$$\mathbf{D} = D_\mathrm{p}\mathbf{I} + \alpha_\mathrm{T}\,|\mathbf{v}|\,\mathbf{I} + \left(\alpha_\mathrm{L} - \alpha_\mathrm{T}\right)\frac{\mathbf{v}^\mathrm{T}\mathbf{v}}{|\mathbf{v}|}, \tag{8}$$

with the pore diffusion coefficient D_p [m^2/s], longitudinal and transversal dispersion coefficients α_L, α_T [m], and pore velocity $\mathbf{v}$ [m/s], i.e., $\mathbf{q} = \phi\mathbf{v}$.

The heterogeneous reaction term is the sum of all mineral dissolution-precipitation reactions that involve the primary species α, which is expressed as

$$R_\alpha^\mathrm{min} = \sum_{m=1}^{N_m} \upsilon_{m\alpha} A_m r_m, \quad \alpha = 1, .., N_p, \tag{9}$$

with the stoichiometric coefficient $\upsilon_{m\alpha}$.

For a mineral, the overall rate of dissolution or precipitation follows the rate law based on transition state theory which is: (Lasaga and Kirkpatrick, 1981; Aagaard and Helgeson, 1982; Steefel and Van Cappellen, 1990; Hellmann and Tisserand, 2006)

$$r_m = k_{+,m} \prod_i a_i^{n_i} \left(1 - \frac{Q_m}{K_{\mathrm{eq},m}}\right), \quad m = 1, .., N_m, \tag{10}$$

where $k_{+,m}$ [mol/m^2/s] is the forward rate constant, a_i is the activity of an inhibiting or catalyzing species raised to the exponent n_i, Q_m [-] is the ion activity product, and $K_{\mathrm{eq},m}$ [-] is the equilibrium constant.

By the law of mass action, the concentration of the secondary species β can be related to the concentration of the primary species α by (Steefel and Lasaga, 1994)

$$\ln a_{s\beta} = -\ln K_{\mathrm{eq},\beta} + \sum_{\alpha=1}^{N_p} \upsilon_{\beta\alpha} \ln a_{p\alpha}, \quad \beta = 1, .., N_s, \tag{11}$$

where $a_{s\beta}$, $a_{p\alpha}$ [-] are the chemical activity with the definition of $a = \gamma \frac{c}{c^\Theta}$. Note that γ [-] is the activity coefficient of an aqueous species, and c^Θ is the standard concentration equal to 1 mol/L.

2.3. Weak formulation

The fluid flow and reactive transport equations can be numerically solved using the finite element method. Thus, we begin by developing their weak forms, using the weighted residual method (Zienkiewicz et al., 2000; Belytschko et al., 2013).

Specifically, Equation (4) is multiplied by a weighting function Ψ^p and then integrated over a bounded domain Ω

$$\int_\Omega \Psi^p S_\mathrm{s} \frac{\partial p}{\partial t}\,\mathrm{d}\Omega + \int_\Omega \Psi^p \nabla\cdot\mathbf{q}\,\mathrm{d}\Omega + \int_\Omega \Psi^p Q_p\,\mathrm{d}\Omega = 0. \tag{12}$$

The domain boundary $\partial\Omega$ consists of two disjoint parts where the Dirichlet and Neumann boundary conditions for the flow problem are respectively imposed, i.e., $\partial\Omega = \Gamma_\mathrm{D}^p \cup \Gamma_\mathrm{N}^p$ and $\Gamma_\mathrm{D}^p \cap \Gamma_\mathrm{N}^p = \emptyset$. For $\forall \mathbf{x} \in \Gamma_\mathrm{D}^p$, $\Psi^p = 0$.

By applying integration by parts to the second term and using the divergence theorem, we obtain

$$\int_\Omega \Psi^p \nabla\cdot\mathbf{q}\,\mathrm{d}\Omega = \int_{\Gamma_\mathrm{N}^p} \Psi^p \mathbf{q}\cdot\mathbf{n}\,\mathrm{d}\Gamma - \int_\Omega \mathbf{q}\cdot\nabla\Psi^p\,\mathrm{d}\Omega. \tag{13}$$

By incorporating Equation (13) into Equation (12), we obtain the weak form of the fluid flow equation

$$\int_\Omega \Psi^p S_s \frac{\partial p}{\partial t}\,\mathrm{d}\Omega + \int_{\Gamma_N^p} \Psi^p \mathbf{q}\cdot\mathbf{n}\,\mathrm{d}\Gamma - \int_\Omega \mathbf{q}\cdot\nabla\Psi^p\,\mathrm{d}\Omega + \int_\Omega \Psi^p Q_p\,\mathrm{d}\Omega = 0. \tag{14}$$

Likewise, the weak form of the reactive transport equation is given as

$$\int_\Omega \Psi^c \phi \frac{\partial c_{T\alpha}}{\partial t}\,\mathrm{d}\Omega + \int_\Omega \Psi^c \frac{\partial \phi}{\partial t} c_{T\alpha}\,\mathrm{d}\Omega + \int_{\Gamma_N^\alpha} \Psi^c \left(\mathbf{q}c_{T\alpha} - \phi\mathbf{D}\nabla c_{T\alpha}\right)\cdot\mathbf{n}\,\mathrm{d}\Gamma - \int_\Omega \left(\mathbf{q}c_{T\alpha} - \phi\mathbf{D}\nabla c_{T\alpha}\right)\cdot\nabla\Psi^c\,\mathrm{d}\Omega + \int_\Omega \Psi^c R_\alpha^{\min}\,\mathrm{d}\Omega = 0. \tag{15}$$

2.4. Boundary conditions

Dirichlet and Neumann boundary conditions typically applied to reactive transport problems are:

$$\begin{aligned} p &= \bar{p} \quad \text{on } \Gamma_D^p, \\ -\mathbf{q}\cdot\mathbf{n} &= \bar{q} \quad \text{on } \Gamma_N^p, \\ c_{T\alpha} &= \bar{c}_{T\alpha} \quad \text{on } \Gamma_D^\alpha, \\ -\left(\mathbf{q}c_{T\alpha} - \phi\mathbf{D}\nabla c_{T\alpha}\right)\cdot\mathbf{n} &= \bar{J}_\alpha \quad \text{on } \Gamma_N^\alpha, \end{aligned} \tag{16}$$

where $\bar{p}$ [Pa] and $\bar{c}_{T\alpha}$ [mol/m^3] are the fixed hydraulic pressure and total concentration of the primary species α at the boundary where Dirichlet constraints apply, $\bar{q}$ [m/s] and $\bar{J}_\alpha$ [mol/m^2/s] are the prescribed seepage velocity and total mass flux, and $\mathbf{n}$ is the outward unit vector normal to the boundary Γ_N.

By incorporating Neumann boundary conditions in Equations (14) and (15), the weak forms become

$$\int_\Omega \Psi^p S_s \frac{\partial p}{\partial t}\,\mathrm{d}\Omega - \int_{\Gamma_N^p} \Psi^p \bar{q}\,\mathrm{d}\Gamma - \int_\Omega \mathbf{q}\cdot\nabla\Psi^p\,\mathrm{d}\Omega + \int_\Omega \Psi^p Q_p\,\mathrm{d}\Omega = 0, \tag{17}$$

$$\int_\Omega \Psi^c \phi \frac{\partial c_{T\alpha}}{\partial t}\,\mathrm{d}\Omega + \int_\Omega \Psi^c \frac{\partial \phi}{\partial t} c_{T\alpha}\,\mathrm{d}\Omega - \int_{\Gamma_N^\alpha} \Psi^c \bar{J}_\alpha\,\mathrm{d}\Gamma - \int_\Omega \left(\mathbf{q}c_{T\alpha} - \phi\mathbf{D}\nabla c_{T\alpha}\right)\cdot\nabla\Psi^c\,\mathrm{d}\Omega + \int_\Omega \Psi^c R_\alpha^{\min}\,\mathrm{d}\Omega = 0. \tag{18}$$

2.5. Finite element discretization

The finite element approximations for the unknown variables p and $c_{T\alpha}$ are given as

$$p \approx \tilde{p} = \mathbf{N}\hat{\mathbf{p}}, \quad c_{T\alpha} \approx \tilde{c}_{T\alpha} = \mathbf{N}\hat{\mathbf{c}}_{T\alpha} \tag{19}$$

where $\tilde{p}$ and $\tilde{c}_{T\alpha}$ are the corresponding approximate solutions, $\mathbf{N}$ is the element shape function vector, $\hat{\mathbf{p}}$ and $\hat{\mathbf{c}}_{T\alpha}$ are the corresponding nodal values in vector form.

In the Bubnov-Galerkin weighted residual method, the weighting function is chosen to be the same as the shape function

$$\Psi^p \approx \mathbf{N}\hat{\boldsymbol{\Psi}}^p, \quad \Psi^c \approx \mathbf{N}\hat{\boldsymbol{\Psi}}^c. \tag{20}$$

By substituting Equations (19) and (20) into their weak forms, the spatially discretized fluid flow equation and reactive transport equation have the following form:

$$\int_\Omega \mathbf{N}^\mathrm{T} S_s \mathbf{N}\,\mathrm{d}\Omega\,\frac{\partial \hat{\mathbf{p}}}{\partial t} - \int_{\Gamma_N^p} \mathbf{N}^\mathrm{T}\bar{q}\,\mathrm{d}\Gamma + \int_\Omega \nabla\mathbf{N}^\mathrm{T}\frac{\mathbf{k}}{\mu}\nabla\mathbf{N}\,\mathrm{d}\Omega\,\hat{\mathbf{p}} - \int_\Omega \nabla\mathbf{N}^\mathrm{T}\frac{\mathbf{k}}{\mu}\rho^l\mathbf{g}\,\mathrm{d}\Omega + \int_\Omega \mathbf{N}^\mathrm{T} Q_p\,\mathrm{d}\Omega = 0. \tag{21}$$

$$\int_\Omega \mathbf{N}^\mathrm{T}\phi\mathbf{N}\,\mathrm{d}\Omega\,\frac{\partial\,\hat{\mathbf{c}}_{T\alpha}}{\partial t} + \int_\Omega \mathbf{N}^\mathrm{T}\frac{\partial\phi}{\partial t}\mathbf{N}\,\mathrm{d}\Omega\,\hat{\mathbf{c}}_{T\alpha} - \int_{\Gamma_N^\alpha} \mathbf{N}^\mathrm{T}\bar{J}_\alpha\,\mathrm{d}\Gamma - \int_\Omega \nabla\mathbf{N}^\mathrm{T}\mathbf{q}\mathbf{N}\,\mathrm{d}\Omega\,\hat{\mathbf{c}}_{T\alpha} + \int_\Omega \nabla\mathbf{N}^\mathrm{T}\phi\mathbf{D}\nabla\mathbf{N}\,\mathrm{d}\Omega\,\hat{\mathbf{c}}_{T\alpha} + \int_\Omega \mathbf{N}^\mathrm{T} R_\alpha^{\min}\,\mathrm{d}\Omega = 0. \tag{22}$$

2.6. Operator splitting approach

Equation (22) could be solved by either the global implicit approach (GIA) or the operator splitting approach (OS). Typically, GIA takes more iterations to reach the solution and is computationally more expensive than OS. Therefore, OS is preferred from the perspective of computational efficiency. In OS, the fully coupled reactive transport process is viewed as a sequential process consisting of a transport stage followed by a reaction stage. Upon time discretization by an implicit backward Euler scheme, Equation (22) is thus split into two discretized systems, which are easier to solve than the original equation directly.

The fully discretized equation for the transport stage is:

$$\int_{\Omega} \mathbf{N}^{\mathrm{T}} \phi \mathbf{N} \, \mathrm{d}\Omega \, \frac{\hat{\mathbf{c}}_{T\alpha}^{\mathrm{transp}} - \hat{\mathbf{c}}_{T\alpha}^{t}}{\Delta t} - \int_{\Gamma_{\mathrm{N}}^{\alpha}} \mathbf{N}^{\mathrm{T}} \bar{J}_{\alpha} \, \mathrm{d}\Gamma - \int_{\Omega} \nabla \mathbf{N}^{\mathrm{T}} \mathbf{q} \mathbf{N} \, \mathrm{d}\Omega \, \hat{\mathbf{c}}_{T\alpha}^{\mathrm{transp}} + \int_{\Omega} \nabla \mathbf{N}^{\mathrm{T}} \phi \mathbf{D} \nabla \mathbf{N} \, \mathrm{d}\Omega \, \hat{\mathbf{c}}_{T\alpha}^{\mathrm{transp}} = 0. \tag{23}$$

The fully discretized equation for the reaction stage is:

$$\int_{\Omega} \mathbf{N}^{\mathrm{T}} \phi \mathbf{N} \, \mathrm{d}\Omega \, \frac{\hat{\mathbf{c}}_{T\alpha}^{t+\Delta t} - \hat{\mathbf{c}}_{T\alpha}^{\mathrm{transp}}}{\Delta t} + \int_{\Omega} \mathbf{N}^{\mathrm{T}} \dot{\phi} \mathbf{N} \, \mathrm{d}\Omega \, \hat{\mathbf{c}}_{T\alpha}^{t+\Delta t} + \int_{\Omega} \mathbf{N}^{\mathrm{T}} R_{\alpha}^{\mathrm{min}} \, \mathrm{d}\Omega = 0. \tag{24}$$

Up to this point, IP-OS development has been completed. We changed the sequence of finite element space discretization and the splitting of transport and reaction operators. Thus, both the transport equation and the reaction equation are spatially discretized based on a uniform mesh. The heterogeneous reaction term $R_{\alpha}^{\mathrm{min}}$ is consequently evaluated at integration points.

2.7. Computational workflow

Figure 1 illustrates the computational workflow of the IP-OS scheme. In the transport stage, Equations (21) and (23) are solved using a staggered coupling scheme until the specified global convergence criteria are met. In the subsequent reaction stage, the obtained intermediate solutions are interpolated element-by-element from nodes to integration points for speciation calculations. Equations (6) and (11) are then solved integration-point-wise using the Newton-Raphson method. Next, Equation (24) is solved using a linear solver, where the heterogeneous reaction term is calculated based on the preceding speciation calculations. Lastly, the transport properties and mineralogical composition of the porous medium are updated accordingly.

In this particular implementation, Phreeqc is chosen for speciation calculations due to its universality. As part of the Phreeqc model setup, the amount of each reactive solid constituent per kilogram of water b_m [mol/kg] is calculated by

$$b_m = \frac{n_m}{m^{\mathrm{l}}} = \frac{\phi_m}{\rho^{\mathrm{l}} \phi V_{\mathrm{m},m}}, \quad m = 1, .., N_m \tag{25}$$

where n_m [mol] is the amount of the solid constituent m and m^{l} [kg] is the mass of pore water.

Also, a simple reactive surface area model is implemented, in which the bulk reactive surface area SA_m [m^2] of the solid constituent m is set proportionally to its bulk volume V_m [m^3]

$$SA_m = s_{\mathrm{s},m} V_m. \tag{26}$$

Equation (26) can be rephrased to relate the bulk reactive surface area to the amount of the solid constituent:

$$SA_m = s_{\mathrm{s},m} V_{\mathrm{m},m} \, b_m \, m^{\mathrm{l}}. \tag{27}$$

By substituting Equation (25) into Equation (27), the expression for bulk reactive surface area is transformed into

$$SA_m = s_{\mathrm{s},m} \frac{\phi_m}{\rho^{\mathrm{l}} \phi} \, m^{\mathrm{l}}. \tag{28}$$

After the execution of Phreeqc, the change of volume fraction of each solid constituent is calculated according to the changes in its amount Δb_m [mol/kg] by

$$\Delta \phi_m = \Delta b_m \, \rho^{\mathrm{l}} \phi V_{\mathrm{m},m}. \tag{29}$$

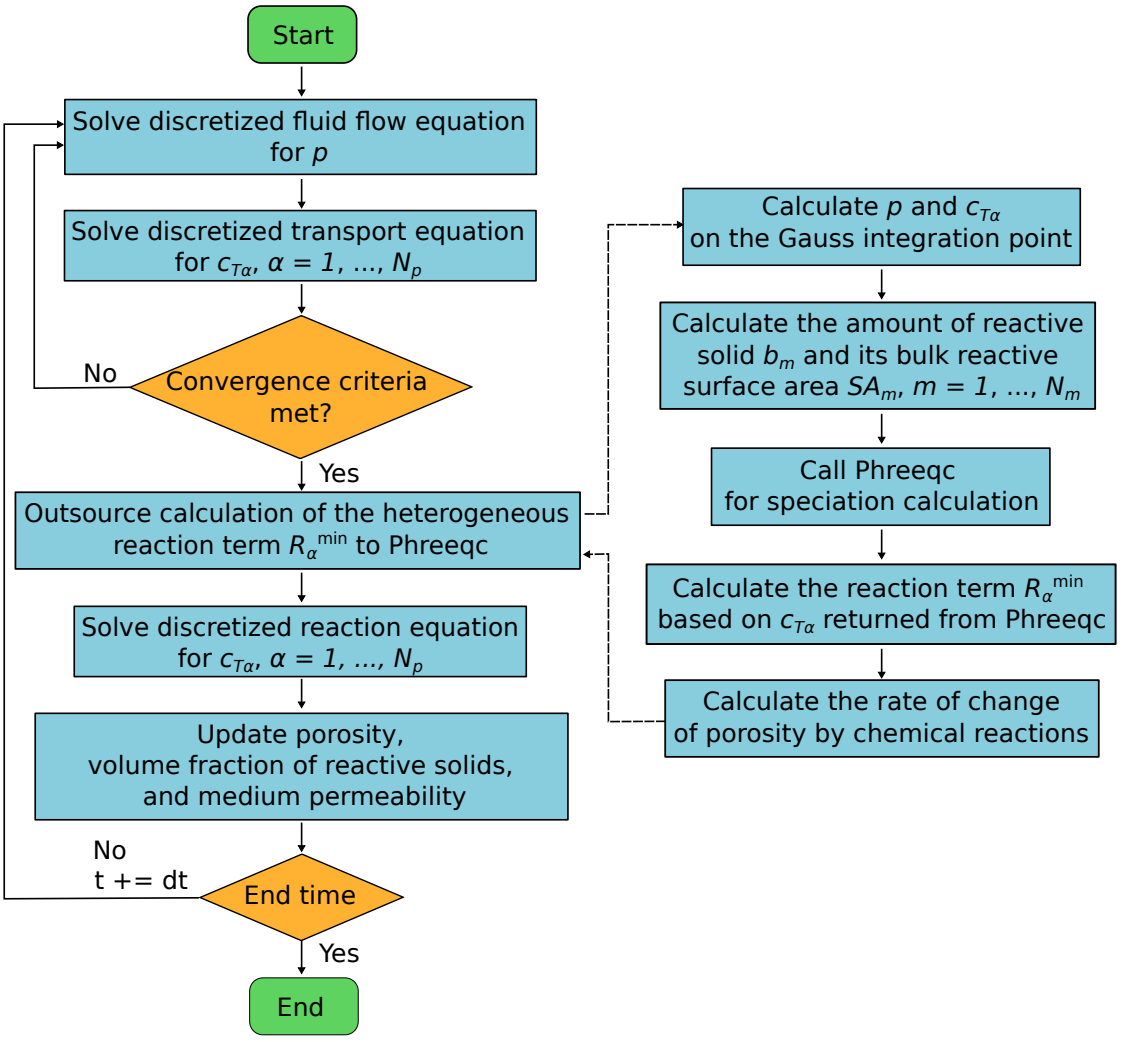

Figure 1: An overview of the computational workflow of the IP-OS scheme.

In order to maintain volume balance, the change in porosity the porosity $\Delta\phi$ [-] is also calculated by

$$\Delta\phi = -\sum_{m=1}^{N_m} \Delta\phi_m. \tag{30}$$

3. Results

3.1. Benchmark I: Biodegradation transport problem

This section examines the advantages and disadvantages of IP-OS in comparison to Nodal-OS using two benchmarks. The first benchmark concerns the transport of dissolved organic matter together with microbial degradation in a semi-infinite saturated porous column. The degradation process is assumed to follow a first-order kinetic law. Here we consider a simple 1D model and assume that microbial degradation will not alter the transport properties of the porous column.

This biodegradation transport problem can be described by Equation (5) in a reduced form as follows:

$$\phi\frac{\partial c}{\partial t} + \nabla\cdot\left(\mathbf{q}c - \phi D_{\mathrm{p}}\nabla c\right) + k_{\mathrm{d}}c = 0, \tag{31}$$

where k_d [1/s] is the first-order decay rate constant. In this case, the governing equation is constrained by the following initial and boundary conditions:

$$\begin{aligned} c(x,0) &= 0, \\ c(0,t) &= 1.0, \\ c(x \to +\infty, t) &= 0. \end{aligned} \tag{32}$$

Table 1
Model parameters used in benchmark I

Parameter	Symbol	Unit	Value
Spatial domain	x	m	[0, 50]
Grid size	Δx	m	0.1
Time interval	t	s	$[0, 9 \cdot 10^5]$
Time step size	Δt	s	$5 \cdot 10^3$
Critical time step size	Δt_{cri}	s	$5 \cdot 10^3$
Pore diffusion coefficient	D_p	m^2/s	$1.157 \cdot 10^{-6}$
Initial porosity	ϕ_0	-	1.0
Darcy flux	q	m/s	$1.157 \cdot 10^{-5}$
First-order decay constant	k_d	1/s	$4.63 \cdot 10^{-5}$
Damköhler number	Da	-	4

Note. The parameter values are mainly sourced from Valocchi and Malmstead (1992).

In the model setting, the ideal semi-infinite porous column is considered to be 50 m, which is long enough to prevent the influence of the no-flux boundary at the far end of the domain. The 1D domain is discretized with 500 line elements of 0.1 m each. The fixed time-stepping scheme is adopted in the simulation. The time step size Δt [s] is set equal to the critical time step size Δt_{cri}, which is determined based on the von Neumann criterion ($\Delta t_{\text{cri}} = \frac{1}{2}\frac{\Delta x^2}{D_p}$). The discretized transport equation and the reaction equation are iteratively solved using the standard Picard method. In both the transport and reaction stages, a uniform relative error tolerance of 10^{-8} is used as the global convergence condition. Table 1 summarizes the parameters used in this benchmark.

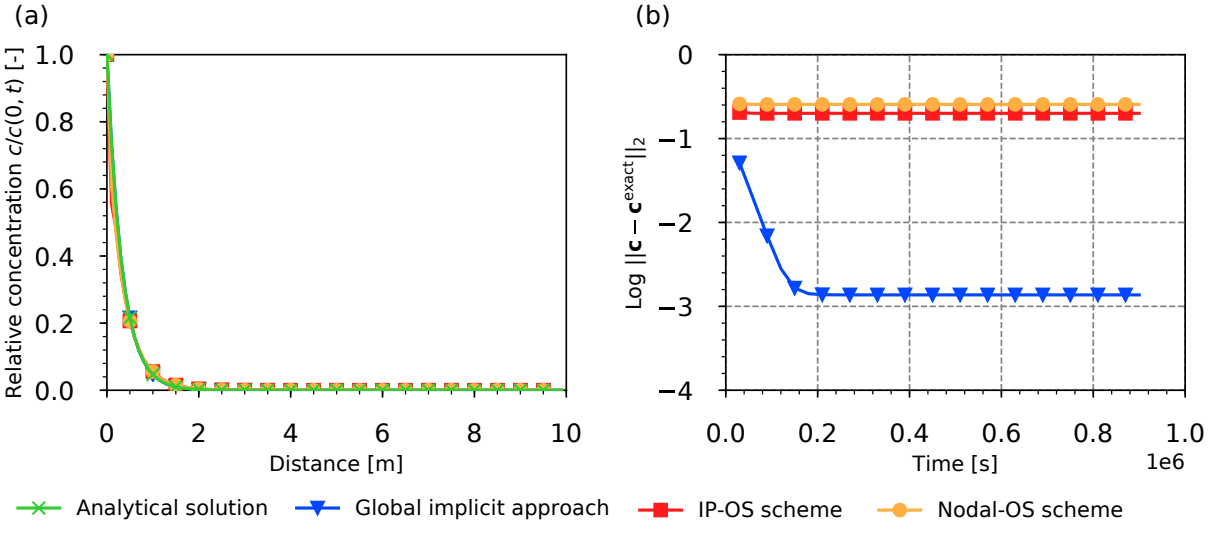

Figure 2: Comparison of different numerical schemes in terms of (a) relative concentration profile at $t = 9 \cdot 10^5$ s; and (b) the L_2 error norm for the concentration field.

Figure 2a shows the concentration profiles of the last time step using Nodal- and IP-OS. Additionally, a numerical solution based on the global implicit approach and the exact analytical solution from Van Genuchten (1981)

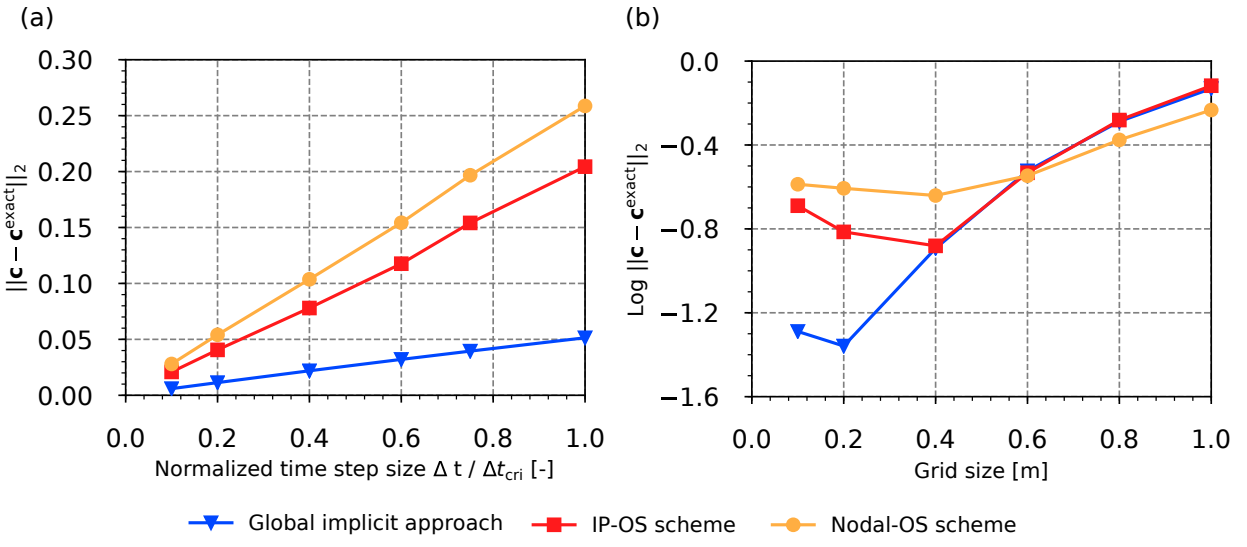

Figure 3: The influences of time step size (a) and grid size (b) on the accuracy of different numerical schemes.

are provided for comparison. As shown in Figure 2a, the presented numerical solutions all agree well with the analytical solution as expected. For each numerical scheme, the Euclidean norm of the approximate solution error $||\mathbf{c} - \mathbf{c}^{\text{exact}}||_2 = \left(\sum_i |c_i - c_i^{\text{exact}}|^2\right)^{1/2}$ over the entire domain is calculated based on the exact analytical solution $\mathbf{c}^{\text{exact}}$. Figure 2b compares the error norms of these numerical schemes. As the simulation time increases, the error norm of the global implicit approach levels off after a decline at the beginning. Its lower bound is in the order of 10^{-3}, which is two orders of magnitude lower than that for Nodal- and IP-OS. This indicates that the global implicit approach is more accurate than the operator splitting approach. Additionally, IP-OS is observed to achieve slightly higher accuracy than the traditional scheme (Nodal-OS). The improvement in accuracy is due to the use of a uniform collocation scheme in space discretization of the transport equation and the reaction equation.

Figure 3 shows the influences of time step size and grid size on the accuracy of three numerical schemes. The error norms are calculated based on the numerical solutions at $t = 3 \cdot 10^4$ s. From Figure 3a, it can be seen that of the three numerical schemes, the global implicit approach is the least sensitive to the time step setting. An increase in time step size results in limited accuracy loss. On the other hand, Nodal- and IP-OS require a much smaller time step size in order to achieve the same accuracy. Between the two OS-FE schemes, IP-OS is always more accurate than Nodal-OS. With increasing time step sizes, the accuracy improvement becomes more pronounced. Figure 3b exhibits the influence of grid size on the accuracy of the three numerical schemes. Note that a fixed time step size of $5 \cdot 10^3$ s is used in the grid convergence test. There is no significant difference between the three schemes for coarse meshes. In all three schemes, moderate mesh refinement improves solution accuracy. However, using a finer mesh than 0.4 m does not affect the accuracy. Further, it is shown that the global implicit approach has the highest attainable accuracy, followed by IP-OS and then Nodal-OS.

3.2. Benchmark II: Matrix acidification in a calcite-containing interlayer

In the second benchmark, we consider a widely observed geochemical scenario where mineral dissolution causes permanent alternations in the transport properties of porous media. For reference purposes, a flow-through column experiment is performed where the porosity and permeability of a calcite-containing interlayer evolve under sulfuric acid attack. Figure 4 gives an overview of the experimental setup which aligns with the previous work of Poonoosamy et al. (2020). The cylindrical reactor has an internal diameter of 0.0099 m and a height of 0.07 m. It is packed from the bottom with layers of quartz sand, sand-calcite mixture, and yet another layer of quartz sand at the top. The packing layers are 0.024 m, 0.022 m, and 0.024 m respectively. The calcite-containing interlayer is formed by mixing quartz sand with the calcite grains at a weight ratio of 2:1. The layered porous column is filled with water before the experiment begins. Once the column is saturated, a 0.005 M sulphuric acid solution (pH = 2.128) is injected through the column

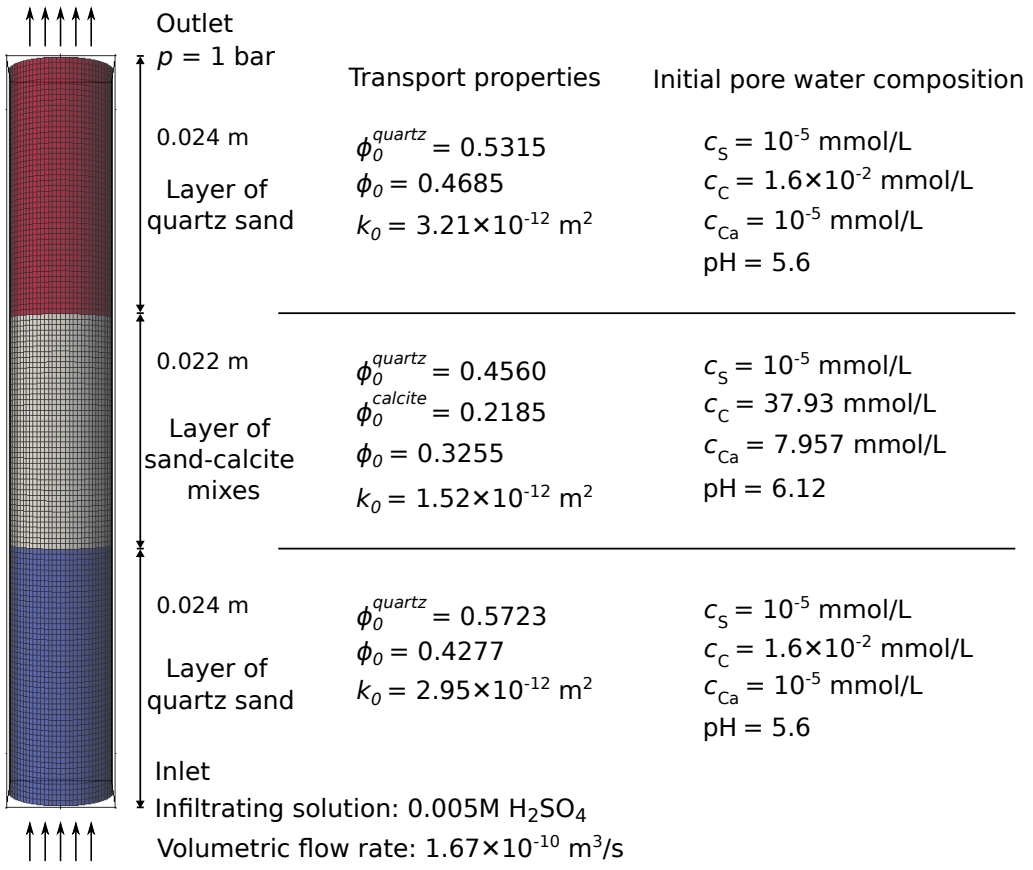

Figure 4: Schematic overview of the flow-through experimental setup along with the transport properties of each packing layers and initial pore water composition.

at a constant volumetric flow rate of $1.67 \cdot 10^{-10}$ m^3/s, resulting in a Darcy flow rate of $2.1695 \cdot 10^{-6}$ m/s. The calcite-containing inter-layer is eroded by the sulphuric acid solution. Note that the initial hydraulic pressure is 1 bar and the downstream pressure is fixed at 1 bar throughout the experiment. The entire flow-through column experiment lasts for 400 hours. Under the prescribed experimental conditions, the dissolved CO_2 produced by the calcite dissolution grows at concentrations below its solubility limit. Thus, no gaseous CO_2 is observed during the experiment. The effluent is sampled from the fluid relief valve once every 24 hours. The collected fluid samples are then analyzed by inductively coupled plasma optical emission spectrometry.

Calcite particles in the interlayer react according to the following reaction pathways (Plummer et al., 1978; Chou et al., 1989; Fazeli et al., 2019)

$$\begin{aligned} &\mathrm{CaCO_3(s) + H^+ \rightleftharpoons Ca^{2+} + HCO_3^+} \\ &\mathrm{CaCO_3(s) + H_2CO_3^* \rightleftharpoons Ca^{2+} + 2\,HCO_3^+} \\ &\mathrm{CaCO_3(s) \rightleftharpoons Ca^{2+} + CO_3^{2-}}, \end{aligned} \tag{33}$$

and the dissolution rate of calcite can be described by the Transition State Theory based kinetic rate law (Palandri and Kharaka, 2004; Molins et al., 2017)

$$r_{\mathrm{calcite}} = \left[k_{\mathrm{acid}}^{298.15} a_{\mathrm{H^+}} + k_{\mathrm{neutral}}^{298.15} + k_{\mathrm{carbonate}}^{298.15} a_{\mathrm{H_2CO_3^*}}\right] \left(1 - \frac{a_{\mathrm{Ca^{2+}}} a_{\mathrm{CO_3^{2-}}}}{K_{\mathrm{eq,calcite}}}\right), \tag{34}$$

where $k_{\mathrm{acid}}^{298.15}$, $k_{\mathrm{neutral}}^{298.15}$, and $k_{\mathrm{carbonate}}^{298.15}$ [mol/m^2/s] are its dissolution rate constants at 25 °C under acid, neutral, and carbonate mechanisms, and a_i [-] is the activity of species i. Note that the logarithms of the calcite dissolution rate con-

stants $\log k_{\text{acid}}^{298.15}$, $\log k_{\text{neutral}}^{298.15}$ and $\log k_{\text{carbonate}}^{298.15}$ are -0.3, -5.81, and -3.48 (Plummer et al., 1978; Palandri and Kharaka, 2004). The equilibrium constant for the reaction $K_{\text{eq,calcite}}$ is equal to $10^{-8.49}$. The LLNL chemical thermodynamic database is employed in the speciation calculations.

Table 2
Model parameters used in benchmark II

Parameter	Symbol	Unit	Value
Spatial domain	x	m	[0, 0.07]
Grid size	Δx	m	$5 \cdot 10^{-4}$
Time interval	t	h	[0, 400]
Time step size	Δt	s	60
Pore diffusion coefficient	D_{p}	m^2/s	10^{-9}
Initial porosity	ϕ_0	-	see Fig. 4
Initial concentration	c_0	mol/m^3	see Fig. 4
Molar volume	V_{m}	m^3/mol	$3.693 \cdot 10^{-5}$
Specific surface area	s_{s}	m^2/m^3	20
Permeability	k	m^2	see Fig. 4
Dynamic viscosity	μ	Pa·s	10^{-3}
Fluid density	ρ^{l}	kg/m^3	10^3
Longitudinal dispersion coefficient	α_{L}	m	10^{-4}

In order to compare the two FE-OS schemes, two one-dimensional reactive transport models are set up using the same spatial and temporal discretization schemes. The layered porous column is discretized into 140 line elements, each with a length of $5 \cdot 10^{-4}$ m. A fixed time step size of 60 s and a relative error tolerance of 10^{-8} are used in the simulations. The flow and transport properties of the individual layers, initial and boundary conditions are partly summarized in Table 2 and also shown in Figure 4.

Given the change in permeability occurring in the interlayer due to calcite dissolution, the evolving permeability is set to be dependent on the porosity, calculated via the Kozeny-Carman relationship. (Kozeny, 1927; Carman, 1937)

$$\mathbf{k} = k_0 \left(\frac{\phi}{\phi_0} \right)^3 \left(\frac{1 - \phi_0}{1 - \phi} \right)^2 \mathbf{I}, \tag{35}$$

with the initial permeability scalar k_0 [m^2] and initial porosity ϕ_0 [-] (see Figure 4).

Figure 5 shows the comparison between simulated and experimental results. Using either Nodal-OS or IP-OS, the measured data can be reproduced well. More specifically, the simulated sulfur breakthrough curves are in excellent agreement with the experimental curve. Since no sulfur is formed during the calcite dissolution, the heterogeneous reaction term is actually absent from the sulfur-specific reaction equation. Thus, neither Nodal-OS nor IP-OS will have an effect on the numerical solution such that the simulated sulfur breakthrough curves are aligned. In addition, no appreciable difference is seen in the simulated calcium breakthrough curves. This implies that the slight accuracy improvement for IP-OS might not be of relevance in realistic applications. The simulated porosity evolution curves also show good agreement with the measured values, despite a slight difference. Such a difference is negligible compared to the measurement error.

Figures 6 presents the simulated spatial distribution of porosity, permeability, and calcite volume fraction. Considering that reactive calcite particles are only present in the interlayer, dissolution and the associated changes in porosity, permeability, and calcite volume fraction should not occur anywhere else. The simulated profiles based on IP-OS (see red curves in Figures 6) are consistent with our priori knowledge that the porosity and permeability of the inert layer remain unchanged. As in IP-OS speciation calculations are performed based on the integration points per element, any resulting changes will not affect adjacent elements. Nodal-OS, on the other hand, shows a different behavior (see blue curves in Figures 6). Porosity and permeability of the inert layers are found to increase in the vicinity of the interface as a result of dissolution in the interlayer. This is due to the fact that Nodal-OS performs speciation calculations on the interface nodes. Following the speciation calculations, the changes in calcite volume fraction are interpolated back to the connected elements from the interface nodes. As the adjacent-interlayer element does not contain calcite, the interpolation operation causes the calcite volume fraction to fall into the negative number range (see the blue curve

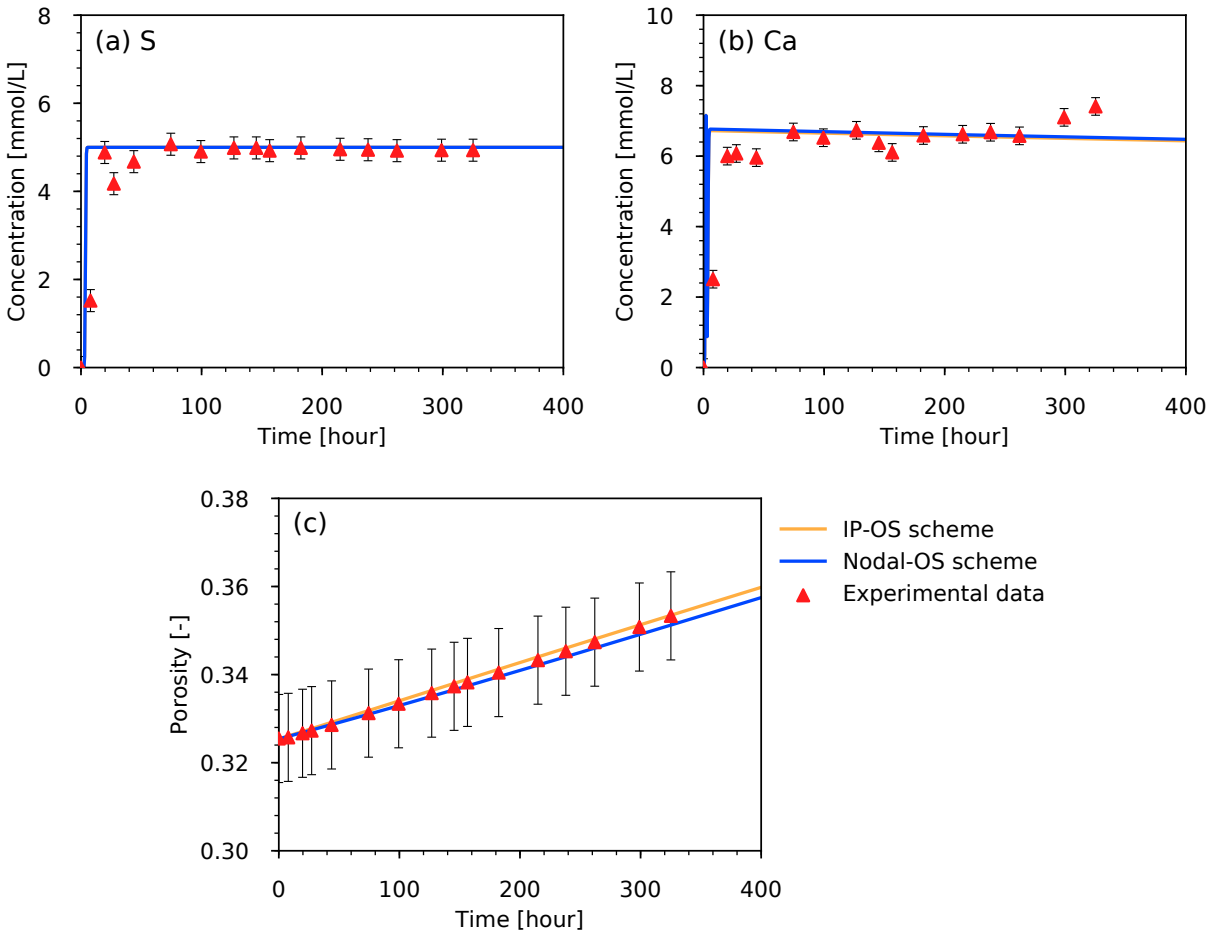

Figure 5: Comparison between the model predictions and experimental measurements: (a) sulfur breakthrough curve; (b) calcium breakthrough curve; and (c) porosity evolution of the inter-layer. Note that the porosity here refers to the overall porosity of the calcite-containing inter-layer. The simulated porosity evolution curves are obtained by the volume-averaging-based homogenization method.

at 0.0235 m and at 0.0465 m in Figure 6c), which is physically unrealistic. Furthermore, this numerical artifact produces unrealistic increases in porosity and permeability in the inert layers. By comparing the two OS-FE schemes, it is evident that IP-OS is superior to Nodal-OS in capturing chemically induced changes in multi-layer heterogeneous systems.

Additionally, it is observed that the undesired numerical artifact extends as far as the length of the adjacent-interface element in the inert layer. To examine the influence of grid size on the numerical artifact, the grid spacing across the inert layers is coarsened from 0.0005 m to 0.003 m. As shown in Figure 7a, the numerical artifact extends further at a coarser grid size. Also, coarser grid spacing causes the porosity increase in the interlayer to be underestimated. Unlike Nodal-OS, increasing the grid spacing has no effect on the porosity profiles simulated by IP-OS (see Figure 7b). These profiles are aligned in the interlayer irrespective of the grid size.

Figure 8 shows the calcium concentration profiles with grid spacings ranging from 0.0005 m to 0.003 m. It is surprising that changing the grid spacing in Nodal-OS results in significant differences between the calculated calcium concentration profiles. Also, a few spikes in Ca are observed across the bottom inert layer. As the grid spacing increases, the spikes appear more frequently and become more pronounced in the inert layer. IP-OS, however, exhibits a more resilient behavior. Increasing the grid spacing has no significant impact on the concentration distribution. This comparison indicates that IP-OS is less sensitive to grid resolution and numerically more stable, whereas using

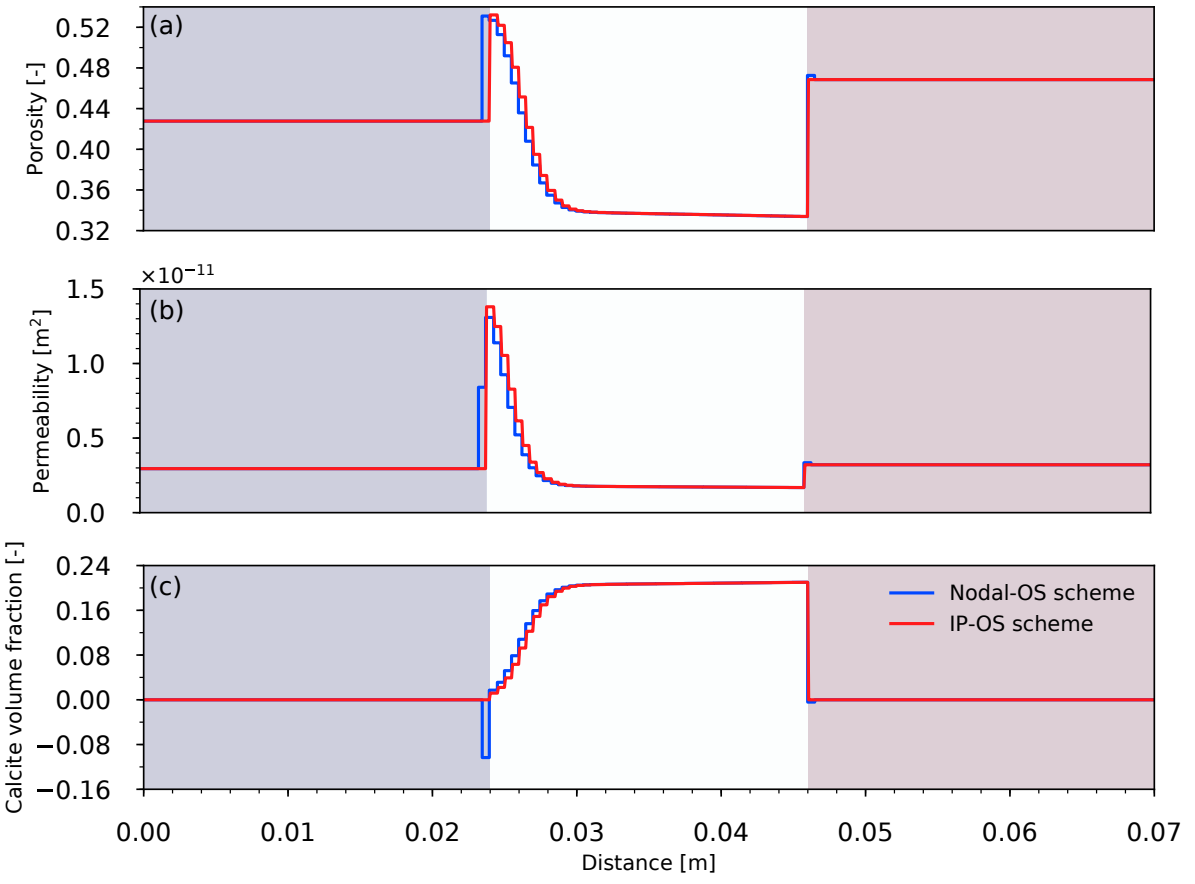

Figure 6: Comparison between the two FE-OS schemes in terms of (a) pore water pressure profile; (b) calcium concentration profile; (c) porosity distribution profile; (d) permeability distribution profile; and (e) calcite particle volume fraction distribution profile. All curves are evaluated at $t = 400$ h.

Nodal-OS may lead to severe mesh dependency issues.

4. Discussion

4.1. Influence of grid irregularity

To further examine the influence of grid irregularity on the numerical artifact, the 1D model is extended to a 3D unstructured grid model. It becomes more evident from the 3D visualization (see Figure 9a) that Nodal-OS results in extensive numerical artifacts in the adjacent interlayer regions. The extent to which the numerical artifacts extend into the inert layer is observed to vary in space. By taking a cross-section of the bottom inert layer in the vicinity of the interface (x = 0.0239 m), we notice that the porosity changes are non-uniformly distributed. This implies that mesh dependency increases in the higher-dimensional simulations due to the grid irregularity effect. On the other hand, the 3D visualization of IP-OS results (see Figure 9b) clearly shows that the porosity across the bilateral inert layers remains well preserved as observed in the 1D model. This indicates that IP-OS is free of such numerical artifacts regardless of dimension.

4.2. Computational performance analysis

Speciation calculations are now performed at integration points rather than at nodes, which will have a significant impact on computational performance. Table 3 summarizes the computational costs of these two OS-FE schemes. As shown in cases 1 and 2, compared to Nodel-OS, the computational cost of IP-OS is doubled since there are twice as

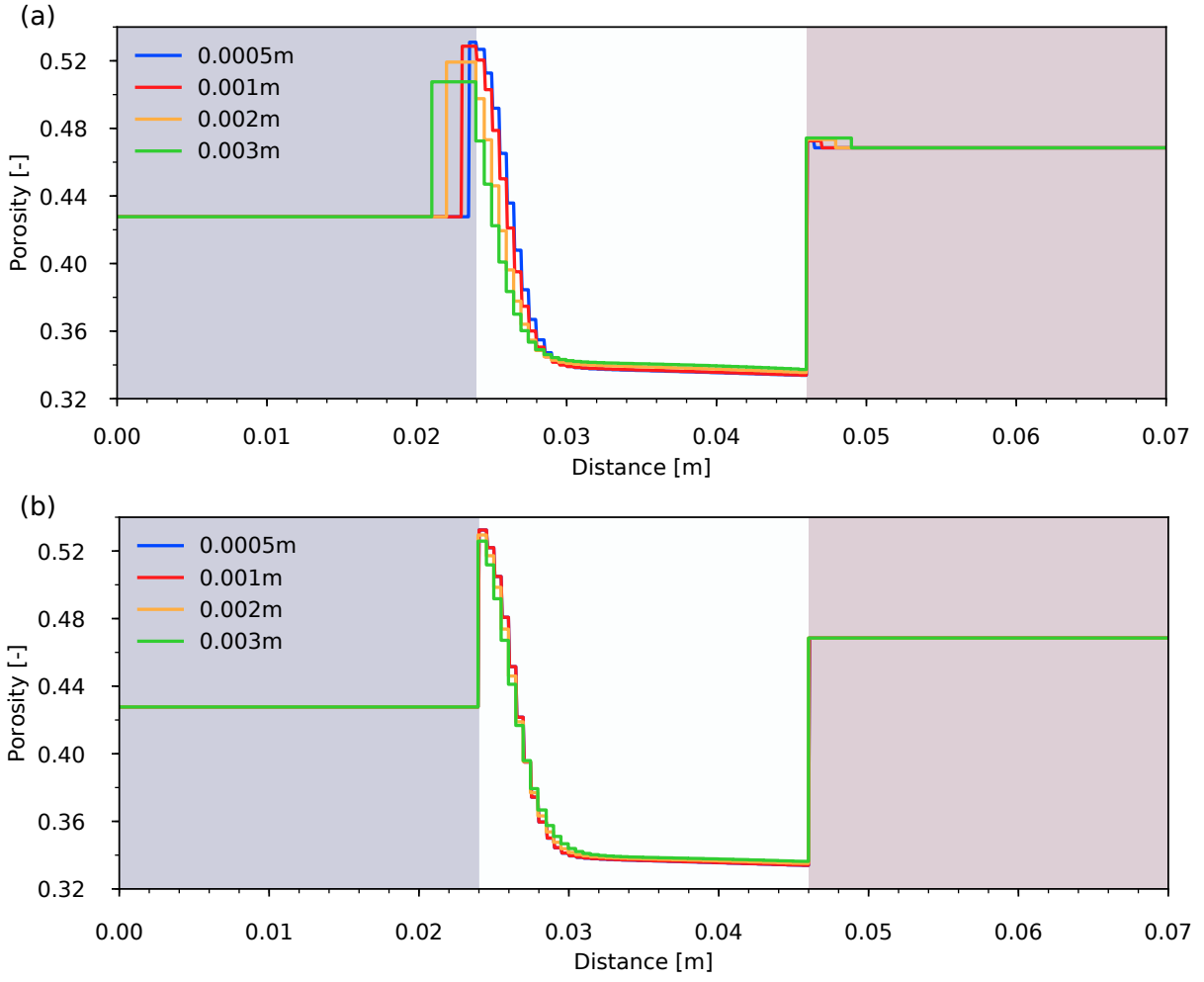

Figure 7: The influence of grid size on the simulated porosity profile ($t = 400\,\mathrm{h}$) with the Nodal-OS scheme (a) and with the IP-OS scheme (b).

many chemical systems to solve. With the extension of the model from 1D to 3D, the number of chemical systems in IP-OS increases dramatically in comparison to Nodal-OS (see cases 3 and 4). Consequently, the computational cost is increased by two orders of magnitude from 2.85 to 414.53 seconds. This indicates that Nodal-OS has a significant performance advantage over IP-OS in the higher-dimensional simulations. Additionally, the computational cost of IP-OS with higher-order quadrature rules is also measured (see cases 5-8). As the number of integration points rises, the computational cost increases in an almost linear manner, while the obtained simulation results are essentially identical. Therefore, IP-OS does not require higher-order quadrature rules.

4.3. Comparison from an implementation perspective

Nodal-OS relies on nodal medium properties to set up chemical systems. Calculating these properties requires three components: 1) the number of elements connected to the node; 2) the volume of each connected element contributing to the node; and 3) extrapolation of bulk medium properties from the integration points of each connected element. As shown in Figure 10, unstructured meshing causes the number of connected elements and their volume contributions to vary from node to node. This makes it more difficult to implement Nodal-OS. After speciation calculations, the changes in nodal medium properties need to be interpolated back to the integration points of each connected element. Thus, implementation of Nodal-OS is rather challenging.

However, IP-OS performs speciation calculations directly on the integration points. It is easy to set up chemical

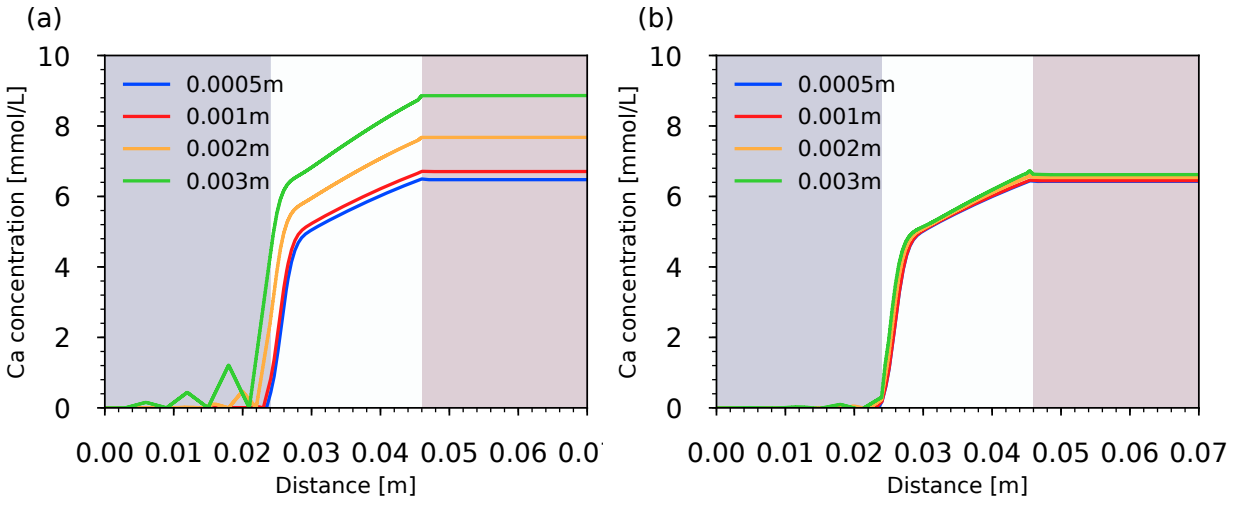

Figure 8: The influence of grid size on the simulated calcium concentration profile ($t = 400$ h) with the Nodal-OS scheme (a) and with the IP-OS scheme (b).

Table 3
Comparison of the computational costs of each OS-FE scheme

Case	Dimension	OS-FE scheme	Number of nodes	Number of elements	Number of integration points per element	Number of chemical systems	Run-time [s]
Case 1	1D	Nodal-OS	141	140	2	141	0.17
Case 2	1D	IP-OS	141	140	2	280	0.35
Case 3	3D	Nodal-OS	1775	8065	5	1775	2.85
Case 4	3D	IP-OS	1775	8065	5	42325	414.53
Case 5	1D	IP-OS	141	140	3	420	0.55
Case 6	1D	IP-OS	141	140	4	560	0.75
Case 7	3D	IP-OS	1775	8065	14	112910	2738.57
Case 8	3D	IP-OS	1775	8065	20	161300	5481.80

systems with bulk medium properties stored on integration points. With IP-OS, neither interpolation/extrapolation nor volume-weighted averaging are required. This makes IP-OS more straightforward than Nodal-OS.

4.4. Applicability of the two OS-FE schemes

By modeling the biodegradation transport problem, we find that IP-OS is only marginally superior to Nodal-OS in terms of accuracy. Nevertheless, Nodal-OS has a considerably better computational performance than IP-OS. In terms of computational efficiency, we recommend using Nodal-OS whenever chemical reactions do not alter transport properties. On the other hand, the simulation of matrix acidification in a layered column shows that the performance of Nodal-OS is less reliable in the multi-layer system, because its results are heavily affected by the grid resolution. As the grid size increases, the simulated effluent calcium concentration starts to deviate from that with the finest grid spacing. In addition, the numerical stability of the Nodal-OS scheme starts to deteriorate with larger grids, and numerical artifacts are also more apparent. In higher-dimensional domains, numerical artifacts are prevalent in the adjacent-interlayer elements. In light of the above facts, we recommend using IP-OS in cases where reactive transport occurs in heterogeneous systems, as well as where chemical reactions change the media properties. It is noteworthy that these problems can also be avoided by using the mixed finite element method, or using the finite volume method.

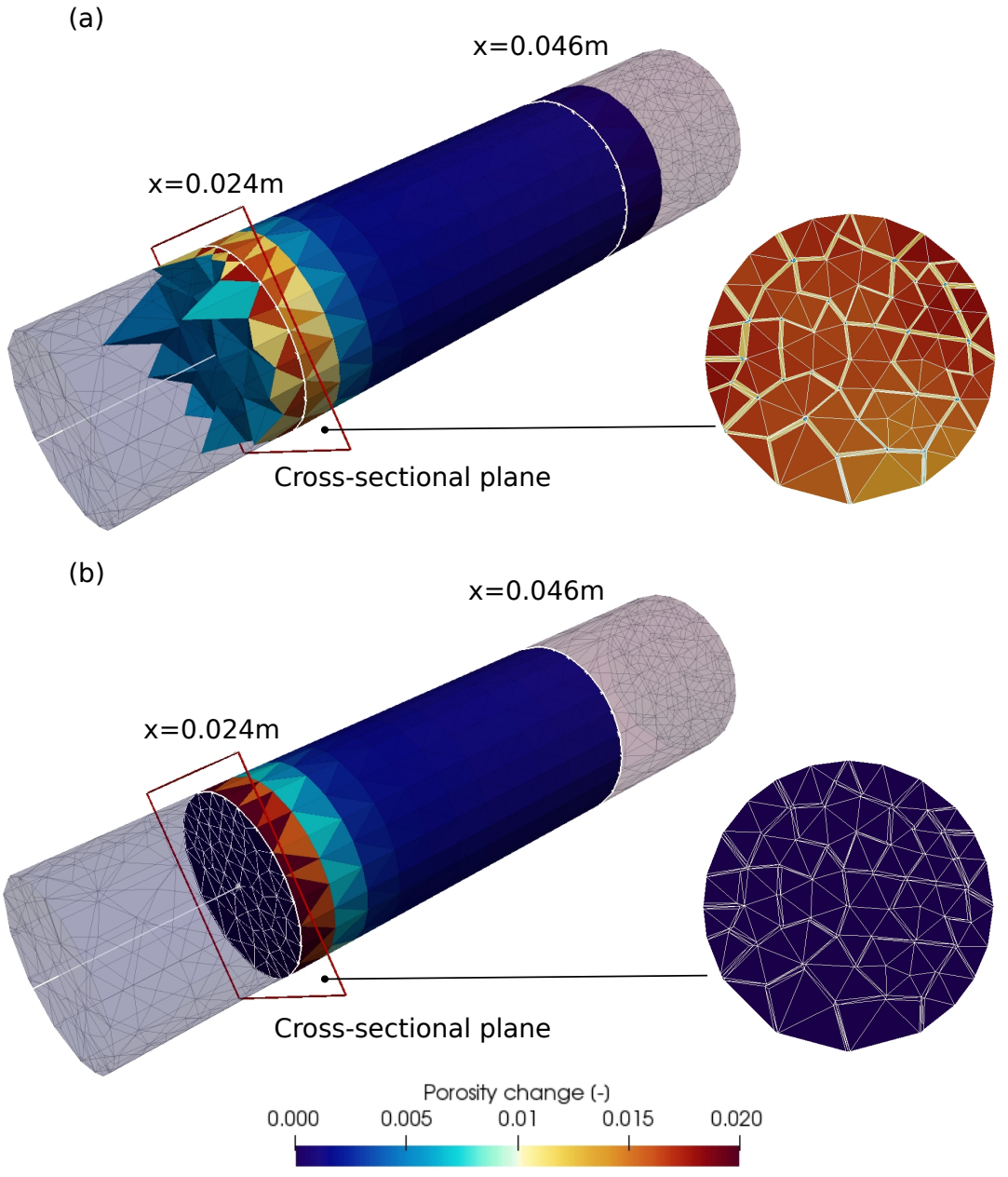

Figure 9: 3-D contour maps of porosity change at a certain time point with the Nodal-OS scheme (a) and with the IP-OS scheme (b).

5. Conclusions

In this study, we developed a new operator-splitting finite element scheme (IP-OS) for reactive transport in saturated porous media. As opposed to the conventional Nodal-OS scheme, the new scheme handles the speciation calculations on integration points, rather than on nodes. This scheme is verified through comparison with an analytical solution of a coupled diffusion-dissolution problem.

Based on this development, the advantages and disadvantages of the IP-OS scheme are discussed using two representative benchmarks. The first one examines a degradation transport problem where microbial degradation reactions

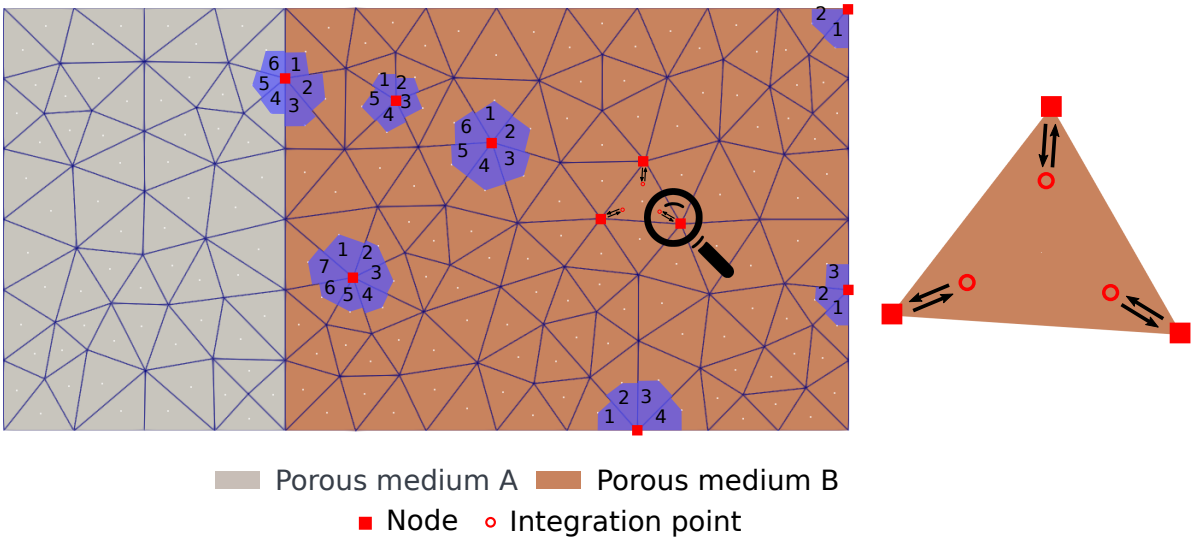

Figure 10: Schematic diagram of the conventional scheme (Nodal-OS). The hatched area represents the nodal control volume.

do not alter transport properties. In the second benchmark, matrix acidification within the calcite-containing interlayer causes porosity changes in a multi-layer column. Additionally, the computational performance of IP-OS and Nodal-OS schemes is analyzed both in 1D and 3D.

To summarize, the IP-OS scheme has the following advantages and disadvantages: (1) IP-OS is superior to Nodal-OS in terms of accuracy; (2) IP-OS is more straightforward to implement; (3) IP-OS is less sensitive to grid resolution, and it is numerically more stable with coarser grid spacing; and (4) IP-OS is computationally more expensive.

Considering the above pros and cons, it is recommended that Nodal-OS be used for cases where chemical reactions do not affect transport properties, and IP-OS for multi-layer heterogeneous cases where chemical reactions alter transport properties.

Computer code availability

The IP-OS scheme proposed in this paper has been integrated into the ComponentTransport Module of the OpenGeosys-6 simulator. The detailed implementation of the scheme can be found at https://github.com/ufz/ogs/tree/master/ProcessLib/ComponentTransport. The sub-library ChemistryLib which provides an interface for interacting with Phreeqc can be accessed at https://github.com/ufz/ogs/tree/master/ChemistryLib.

CRediT authorship contribution statement

Renchao Lu: Conceptualization of this study, Algorithm development and implementation, Benchmark definition, Result analysis, and Drafting of the manuscript. Thomas Nagel and Haibing Shao: Algorithm development, Benchmark definition, and Result analysis. Jenna Poonoosamy: Benchmark definition and Curation of the experiment. Dmitri Namov and Thomas Fischer: Software development and Algorithm implementation. Olaf Kolditz and Vanessa Montoya: Benchmark definition and Result analysis. All the authors contributed to the writing of the manuscript.

Declaration of competing interest

The authors declare that they have no known competing financial interests or personal relationships that could have appeared to influence the work reported in this paper.

Acknowledgments

We would like to thank the three anonymous reviewers for improving this paper. We acknowledge the funding support by the iCROSS-Project (Integrity of nuclear waste repository systems – Cross-scale system understanding and analysis) by the Federal Ministry of Research and Education (BMBF) (grant number 02NUK053E) and the Helmholtz Association (Helmholtz-Gemeinschaft e.V.) through the Impulse and Networking Funds (grant number SO-093). We are also grateful for the support from the Federal Ministry of Education and Research (BMBF) for the GeomInt2 project (grant number 03G0899D). In addition, this work has received funding from the European Union's Horizon 2020 research and innovation programme 2014-2018 under grant agreement ID: 847593 - European Joint Programme on Radioactive Waste Management (EURAD), in particular from the work packages ACED and DONUT.

A. Verification of implementation

Consider an aqueous species B_1 diffuses in a five-centimeter-long porous column ($L = 0.05\,\mathrm{m}$). The diffusive transport of the species B_1 is accompanied by dissolution of the solid constituent $M_{(s)}$. A mole of the solid $M_{(s)}$ that dissolves will produce one mole species B_1 plus one mole species B_2 according to the chemical equation

$$M_{(s)} \rightleftharpoons B_1 + B_2. \tag{36}$$

Note that no other chemical reactions (e.g., homogeneous aqueous reactions) are considered further.

The dissolution kinetics is governed by the following rate law: (Hayek et al., 2011)

$$r_{M_{(s)}} = k_+ \left[1 - \frac{f(x)\, c_1}{K}\right], \tag{37}$$

where K [mol/m^3] is its solubility product constant, c_1 and $f(x)$ [mol/m^3] are respectively the molar concentrations of species B_1 and B_2.

Additionally, we assume that the concentration of species B_2 is fixed in space and maintained constant over time without taking into account the spatial and temporal evolution caused by migration and mineral dissolution. Hayek et al. (2011) argued that this assumption facilitates the derivation of the analytical solution, despite its limited use in natural systems. As shown in Figure 11, the time-invariant B_2 concentration profile is expressed as a function of position x:

$$f(x) = \frac{\beta}{1 + \exp\left[\gamma\,(x - \lambda)\right]}, \tag{38}$$

with the arbitrary constants β, γ, and λ [-].

This diffusion-dissolution system can be described by a reduced form of Equation (5) as (Hayek et al., 2011)

$$\frac{\partial\left(\phi c_1\right)}{\partial t} - \nabla\cdot\left(\phi \mathbf{D}\nabla c_1\right) + s_s \phi r_{M_{(s)}} = 0. \tag{39}$$

Below are the initial and boundary conditions at $x = 0$ and $x = L$:

$$\begin{aligned}
c_1(x,0) &= \theta \exp\left(-\alpha x\right), \\
c_1(0,t) &= \frac{K\left[V_m c_1(0,0) - 1\right] - \left[f(0)c_1(0,0) - K\right]\exp\left\{-\dfrac{k_+ s_s\left[f(0) - KV_m\right]t}{K}\right\}}{f(0)\left[V_m c_1(0,0) - 1\right] - V_m\left[f(0)c_1(0,0) - K\right]\exp\left\{-\dfrac{k_+ s_s\left[f(0) - KV_m\right]t}{K}\right\}}, \\
c_1(L,t) &= \frac{K\left[V_m c_1(L,0) - 1\right] - \left[f(L)c_1(L,0) - K\right]\exp\left\{-\dfrac{k_+ s_s\left[f(L) - KV_m\right]t}{K}\right\}}{f(L)\left[V_m c_1(L,0) - 1\right] - V_m\left[f(L)c_1(L,0) - K\right]\exp\left\{-\dfrac{k_+ s_s\left[f(L) - KV_m\right]t}{K}\right\}},
\end{aligned} \tag{40}$$

Table 4
Model parameters used in the verification test

Parameter	Symbol	Unit	Value
Spatial domain	x	m	[0, 0.05]
Grid size	Δx	m	10^{-4}
Time interval	t	hour	[0, 10^4]
Time step size	Δt	s	10
Pore diffusion coefficient	D_p	m^2/s	10^{-11}
Initial porosity	ϕ_0	-	0.5
Molar volume	V_m	$\mathrm{m}^3/\mathrm{mol}$	1.0
Specific surface area	s_s	$\mathrm{m}^2/\mathrm{m}^3$	$3 \cdot 10^4$
	α	-	10^3
	β	-	0.1
Arbitary constants	λ	-	10^{-2}
	γ	-	$-5 \cdot 10^3$
	θ	-	0.2
Solubility product constant	K	$\mathrm{mol}/\mathrm{m}^3$	$10^{-10.05}$
Dissolution rate constant	k^+	$\mathrm{mol}/\mathrm{m}^2/\mathrm{s}$	$6 \cdot 10^{-10}$

Note. The parameter values are sourced from Hayek et al. (2011).

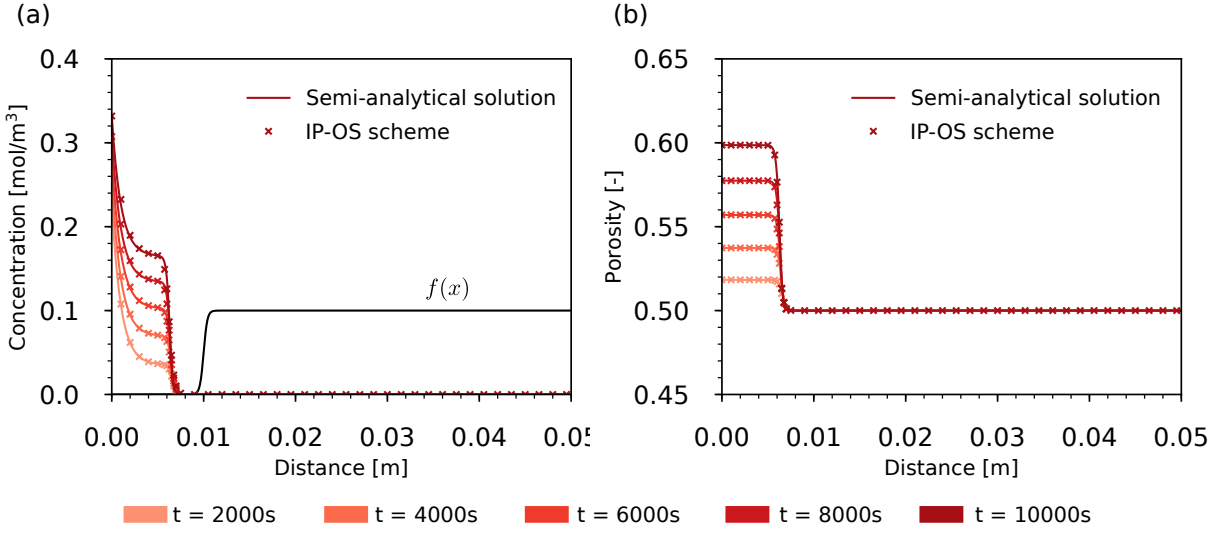

Figure 11: Comparison between the numerical and analytical solutions in terms of (a) species B_1 concentration profile; and (b) porosity distribution profile.

with the arbitrary constants θ and α [-].

Figure 11a displays the computed B_1 concentration profiles along with the analytical solutions, with the colors representing the concentration profiles at different time points. As a result of its low effective diffusivity, the species B_1 is largely retained near the inlet of the column. Thus, the resulting solute accumulation slows down the dissolution rate of the solid $M_{(\mathrm{s})}$. Similarly, Figure 11b shows the computed profiles of porosity along with the corresponding analytical solutions. In the absence of species nearby the inlet, the porosity increases equally across the space due to uniform dissolution. However, in the remaining region, the porosity remains constant due to the relatively high B_2 concentration which prevents the solid from dissolving. Additionally, all simulation results agree well with the analytical results. By comparing spatio-temporal evolution of the B_1 concentration and porosity, it is confirmed that the implementation of the IP-OS scheme is correct.

References

Aagaard, P., Helgeson, H.C., 1982. Thermodynamic and kinetic constraints on reaction rates among minerals and aqueous solutions; i, theoretical considerations. American Journal of Science 282, 237–285.

Azad, V.J., Li, C., Verba, C., Ideker, J.H., Isgor, O.B., 2016. A COMSOL–GEMS interface for modeling coupled reactive-transport geochemical processes. Computers & Geosciences 92, 79–89.

Bächler, D., Kohl, T., 2005. Coupled thermal–hydraulic–chemical modelling of enhanced geothermal systems. Geophysical Journal International 161, 533–548.

Ballarini, E., Beyer, C., Bauer, R., Griebler, C., Bauer, S., 2014. Model based evaluation of a contaminant plume development under aerobic and anaerobic conditions in 2D bench-scale tank experiments. Biodegradation 25, 351–371.

Barry, D., Miller, C., Culligan-Hensley, P., 1996. Temporal discretisation errors in non-iterative split-operator approaches to solving chemical reaction/groundwater transport models. Journal of Contaminant Hydrology 22, 1–17.

Bea, S., Ayora, C., Carrera, J., Saaltink, M., Dold, B., 2010. Geochemical and environmental controls on the genesis of soluble efflorescent salts in coastal mine tailings deposits: A discussion based on reactive transport modeling. Journal of Contaminant Hydrology 111, 65–82.

Bell, L., Binning, P.J., 2004. A split operator approach to reactive transport with the forward particle tracking eulerian lagrangian localized adjoint method. Advances in Water Resources 27, 323–334.

Belytschko, T., Liu, W.K., Moran, B., Elkhodary, K., 2013. Nonlinear finite elements for continua and structures. John wiley & sons.

Berner, U., Kulik, D.A., Kosakowski, G., 2013. Geochemical impact of a low-pH cement liner on the near field of a repository for spent fuel and high-level radioactive waste. Physics and Chemistry of the Earth, Parts A/B/C 64, 46–56.

Beyer, C., Li, D., De Lucia, M., Kühn, M., Bauer, S., 2012. Modelling CO_2–induced fluid–rock interactions in the Altensalzwedel gas reservoir. Part II: coupled reactive transport simulation. Environmental Earth Sciences 67, 573–588.

Bilke, L., Flemisch, B., Kalbacher, T., Kolditz, O., Helmig, R., Nagel, T., 2019. Development of open-source porous media simulators: principles and experiences. Transport in Porous Media 130, 337–361.

Bonte, M., Stuyfzand, P.J., Breukelen, B.M.v., 2014. Reactive transport modeling of thermal column experiments to investigate the impacts of aquifer thermal energy storage on groundwater quality. Environmental Science & Technology 48, 12099–12107.

Boog, J., Kalbacher, T., Nivala, J., Forquet, N., van Afferden, M., Müller, R.A., 2019. Modeling the relationship of aeration, oxygen transfer and treatment performance in aerated horizontal flow treatment wetlands. Water Research 157, 321–334.

Boog, J., Nivala, J., Kalbacher, T., van Afferden, M., Mueller, R.A., 2020. Do wastewater pollutants impact oxygen transfer in aerated horizontal flow wetlands? Chemical Engineering Journal 383, 123173.

Brunner, F., Knabner, P., 2019. A global implicit solver for miscible reactive multiphase multicomponent flow in porous media. Computational Geosciences 23, 127–148.

Carman, P.C., 1937. Fluid flow through granular beds. Trans. Inst. Chem. Eng. 15, 150–166.

Carrayrou, J., Hoffmann, J., Knabner, P., Kräutle, S., De Dieuleveult, C., Erhel, J., Van Der Lee, J., Lagneau, V., Mayer, K.U., Macquarrie, K.T., 2010. Comparison of numerical methods for simulating strongly nonlinear and heterogeneous reactive transport problems—the MoMaS benchmark case. Computational Geosciences 14, 483–502.

Carrayrou, J., Mosé, R., Behra, P., 2004. Operator-splitting procedures for reactive transport and comparison of mass balance errors. Journal of Contaminant Hydrology 68, 239–268.

Celia, M.A., Bouloutas, E.T., Zarba, R.L., 1990. A general mass-conservative numerical solution for the unsaturated flow equation. Water Resources Research 26, 1483–1496.

Chen, Y., Xu, W., Ling, D., Zhan, L., Gao, W., 2020. A degradation–consolidation model for the stabilization behavior of landfilled municipal solid waste. Computers & Geotechnics 118, 103341.

Chen, Z., Ewing, R.E., 1997. Stability and convergence of a finite element method for reactive transport in ground water. SIAM Journal on Numerical Analysis 34, 881–904.

Chiang, C.Y., Dawson, C.N., Wheeler, M.F., 1991. Modeling of in-situ biorestoration of organic compounds in groundwater. Transport in Porous Media 6, 667–702.

Chou, L., Garrels, R.M., Wollast, R., 1989. Comparative study of the kinetics and mechanisms of dissolution of carbonate minerals. Chemical Geology 78, 269–282.

Cirpka, O.A., Frind, E.O., Helmig, R., 1999. Numerical methods for reactive transport on rectangular and streamline-oriented grids. Advances in Water Resources 22, 711–728.

Damiani, L.H., Kosakowski, G., Glaus, M.A., Churakov, S.V., 2020. A framework for reactive transport modeling using FEniCS–Reaktoro: governing equations and benchmarking results. Computational Geosciences , 1–15.

Druhan, J.L., Tournassat, C., 2019. Preface. Reviews in Mineralogy and Geochemistry 85, IV–V. doi:10.2138/rmg.2019.85.0.

Elakneswaran, Y., Ishida, T., 2014. Development and verification of an integrated physicochemical and geochemical modelling framework for performance assessment of cement-based materials. Journal of Advanced Concrete Technology 12, 111–126.

Estep, D., Ginting, V., Ropp, D., Shadid, J.N., Tavener, S., 2008. An a posteriori–a priori analysis of multiscale operator splitting. SIAM Journal on Numerical Analysis 46, 1116–1146.

Ewing, R., Lazarov, R., Lin, Y., 2000. Finite volume element approximations of nonlocal reactive flows in porous media. Numerical Methods for Partial Differential Equations: An International Journal 16, 285–311.

Ewing, R.E., Wang, H., 2001. A summary of numerical methods for time-dependent advection-dominated partial differential equations. Journal of Computational and Applied Mathematics 128, 423–445.

Fahs, M., Carrayrou, J., Younes, A., Ackerer, P., 2008. On the efficiency of the direct substitution approach for reactive transport problems in porous media. Water, Air, and Soil Pollution 193, 299–308.

Fazeli, H., Patel, R.A., Ellis, B.R., Hellevang, H., 2019. Three-dimensional pore-scale modeling of fracture evolution in heterogeneous carbonate caprock subjected to CO_2-enriched brine. Environmental Science & Technology 53, 4630–4639.

Fumagalli, A., Scotti, A., 2021. A mathematical model for thermal single-phase flow and reactive transport in fractured porous media. Journal of Computational Physics 434, 110205.

Gamazo, P., Slooten, L.J., Carrera, J., Saaltink, M.W., Bea, S., Soler, J., 2016. Proost: object-oriented approach to multiphase reactive transport modeling in porous media. Journal of Hydroinformatics 18, 310–328.

Geiser, J., 2011. Iterative splitting methods for differential equations. CRC Press.

Georget, F., Prévost, J.H., Huet, B., 2017. A reactive transport simulator for variable porosity problems. Computational Geosciences 21, 95–116.

Gin, S., Abdelouas, A., Criscenti, L.J., Ebert, W.L., Ferrand, K., Geisler, T., Harrison, M.T., Inagaki, Y., Mitsui, S., Mueller, K.T., et al., 2013. An international initiative on long-term behavior of high-level nuclear waste glass. Materials Today 16, 243–248.

Guo, B., Hong, Y., Qiao, G., Ou, J., 2018. A COMSOL-PHREEQC interface for modeling the multi-species transport of saturated cement-based materials. Construction and Building Materials 187, 839–853.

Hayek, M., Kosakowski, G., Churakov, S., 2011. Exact analytical solutions for a diffusion problem coupled with a precipitation-dissolution reaction and feedback of porosity change. Water Resources Research 47.

He, W., Beyer, C., Fleckenstein, J., Jang, E., Kolditz, O., Naumov, D., Kalbacher, T., 2015. A parallelization scheme to simulate reactive transport in the subsurface environment with OGS#IPhreeqc 5.5.7-3.1.2. Geoscientific Model Development 8, 3333.

Hellmann, R., Tisserand, D., 2006. Dissolution kinetics as a function of the gibbs free energy of reaction: An experimental study based on albite feldspar. Geochimica et Cosmochimica Acta 70, 364–383.

Hoffmann, J., Kräutle, S., Knabner, P., 2010. A parallel global-implicit 2-D solver for reactive transport problems in porous media based on a reduction scheme and its application to the MoMaS benchmark problem. Computational Geosciences 14, 421–433.

Huang, Y., Shao, H., Wieland, E., Kolditz, O., Kosakowski, G., 2018. A new approach to coupled two-phase reactive transport simulation for long-term degradation of concrete. Construction and Building Materials 190, 805–829.

Idiart, A., Laviña, M., Kosakowski, G., Cochepin, B., Meeussen, J.C., Samper, J., Mon, A., Montoya, V., Munier, I., Poonoosamy, J., et al., 2020. Reactive transport modelling of a low-pH concrete/clay interface. Applied Geochemistry , 104562.

Illiano, D., Pop, I.S., Radu, F.A., 2021. Iterative schemes for surfactant transport in porous media. Computational Geosciences 25, 805–822.

Jacques, D., Šimůnek, J., 2005. User manual of the multicompenent variably-saturated flow and transport model HP1. Technical Report. SCK-CEN.

Jacques, D., Šimůnek, J., Mallants, D., Van Genuchten, M.T., 2006. Operator-splitting errors in coupled reactive transport codes for transient variably saturated flow and contaminant transport in layered soil profiles. Journal of Contaminant Hydrology 88, 197–218.

Kanney, J.F., Miller, C.T., Kelley, C., 2003. Convergence of iterative split-operator approaches for approximating nonlinear reactive transport problems. Advances in Water Resources 26, 247–261.

Kirkner, D.J., Reeves, H., 1988. Multicomponent mass transport with homogeneous and heterogeneous chemical reactions: effect of the chemistry on the choice of numerical algorithm: 1. theory. Water Resources Research 24, 1719–1729.

Kolditz, O., Bauer, S., Bilke, L., Böttcher, N., Delfs, J.O., Fischer, T., Görke, U.J., Kalbacher, T., Kosakowski, G., McDermott, C., et al., 2012. OpenGeoSys: an open-source initiative for numerical simulation of thermo-hydro-mechanical/chemical (THM/C) processes in porous media. Environmental Earth Sciences 67, 589–599.

Kosakowski, G., Berner, U., 2013. The evolution of clay rock/cement interfaces in a cementitious repository for low-and intermediate level radioactive waste. Physics and Chemistry of the Earth, Parts A/B/C 64, 65–86.

Kosakowski, G., Berner, U., Wieland, E., Glaus, M., Degueldre, C., 2014. Geochemical evolution of the L/ILW near-field. Technical Report. Paul Scherrer Institute (PSI).

Kosakowski, G., Watanabe, N., 2014. OpenGeoSys-Gem: a numerical tool for calculating geochemical and porosity changes in saturated and partially saturated media. Physics and Chemistry of the Earth, Parts A/B/C 70, 138–149.

Kozeny, J., 1927. Uber kapillare leitung der wasser in boden. Royal Academy of Science, Vienna, Proc. Class I 136, 271–306.

Kräutle, S., Knabner, P., 2007. A reduction scheme for coupled multicomponent transport-reaction problems in porous media: Generalization to problems with heterogeneous equilibrium reactions. Water Resources Research 43.

Kulik, D.A., Wagner, T., Dmytrieva, S.V., Kosakowski, G., Hingerl, F.F., Chudnenko, K.V., Berner, U.R., 2013. GEM-Selektor geochemical modeling package: revised algorithm and GEMS3K numerical kernel for coupled simulation codes. Computational Geosciences 17, 1–24.

Lasaga, A.C., Kirkpatrick, R.J., 1981. Kinetics of geochemical processes .

Leal, A.M., Kulik, D.A., Smith, W.R., Saar, M.O., 2017. An overview of computational methods for chemical equilibrium and kinetic calculations for geochemical and reactive transport modeling. Pure and Applied Chemistry 89, 597–643.

Li, D., Bauer, S., Benisch, K., Graupner, B., Beyer, C., 2014. OpenGeoSys-ChemApp: a coupled simulator for reactive transport in multiphase systems and application to CO_2 storage formation in Northern germany. Acta Geotechnica 9, 67–79.

Lichtner, P.C., 1985. Continuum model for simultaneous chemical reactions and mass transport in hydrothermal systems. Geochimica et Cosmochimica Acta 49, 779–800.

Lichtner, P.C., 1996. Continuum formulation of multicomponent-multiphase reactive transport. Reviews in Mineralogy 34, 1–82.

List, F., Radu, F.A., 2016. A study on iterative methods for solving richards' equation. Computational Geosciences 20, 341–353.

Mayer, K.U., MacQuarrie, K.T., 2010. Solution of the momas reactive transport benchmark with min3p—model formulation and simulation results. Computational Geosciences 14, 405–419.

Meeussen, J.C., 2003. Orchestra: An object-oriented framework for implementing chemical equilibrium models. Environmental Science & Technology 37, 1175–1182.

Miller, C.T., Dawson, C.N., Farthing, M.W., Hou, T.Y., Huang, J., Kees, C.E., Kelley, C., Langtangen, H.P., 2013. Numerical simulation of water resources problems: Models, methods, and trends. Advances in Water Resources 51, 405–437.

Mitra, K., Pop, I.S., 2019. A modified l-scheme to solve nonlinear diffusion problems. Computers & Mathematics with Applications 77, 1722–1738.

Molins, S., Carrera, J., Ayora, C., Saaltink, M.W., 2004. A formulation for decoupling components in reactive transport problems. Water Resources Research 40.

Molins, S., Knabner, P., 2019. Multiscale approaches in reactive transport modeling. Reviews in Mineralogy and Geochemistry 85, 27–48.

Molins, S., Trebotich, D., Miller, G.H., Steefel, C.I., 2017. Mineralogical and transport controls on the evolution of porous media texture using direct numerical simulation. Water Resources Research 53, 3645–3661.

Muniruzzaman, M., Rolle, M., 2016. Modeling multicomponent ionic transport in groundwater with iphreeqc coupling: Electrostatic interactions and geochemical reactions in homogeneous and heterogeneous domains. Advances in Water Resources 98, 1–15.

Nagel, T., Beckert, S., Lehmann, C., Gläser, R., Kolditz, O., 2016. Multi-physical continuum models of thermochemical heat storage and transformation in porous media and powder beds—a review. Applied Energy 178, 323–345.

Nardi, A., Idiart, A., Trinchero, P., de Vries, L.M., Molinero, J., 2014. Interface COMSOL-PHREEQC (iCP), an efficient numerical framework for the solution of coupled multiphysics and geochemistry. Computers & Geosciences 69, 10–21.

Palandri, J.L., Kharaka, Y.K., 2004. A compilation of rate parameters of water-mineral interaction kinetics for application to geochemical modeling. Technical Report. Geological Survey Menlo Park CA.

Parkhurst, D.L., Appelo, C., 2013. Description of input and examples for PHREEQC version 3: a computer program for speciation, batch-reaction, one-dimensional transport, and inverse geochemical calculations. Technical Report. US Geological Survey.

Plummer, L., Wigley, T., Parkhurst, D., 1978. The kinetics of calcite dissolution in CO_2-water systems at 5° to 60°C and 0.0 to 1.0 atm CO_2. American Journal of Science 278, 179–216.

Poonoosamy, J., Haber-Pohlmeier, S., Deng, H., Deissmann, G., Klinkenberg, M., Gizatullin, B., Stapf, S., Brandt, F., Bosbach, D., Pohlmeier, A., 2020. Combination of mri and sem to assess changes in the chemical properties and permeability of porous media due to barite precipitation. Minerals 10, 226.

Poonoosamy, J., Wanner, C., Epping, P.A., Águila, J., Samper, J., Montenegro, L., Xie, M., Su, D., Mayer, K., Mäder, U., et al., 2018. Benchmarking of reactive transport codes for 2D simulations with mineral dissolution–precipitation reactions and feedback on transport parameters. Computational Geosciences , 1–22.

Pruess, K., García, J., Kovscek, T., Oldenburg, C., Rutqvist, J., Steefel, C., Xu, T., 2004. Code intercomparison builds confidence in numerical simulation models for geologic disposal of CO_2. Energy 29, 1431–1444.

Reed, M.H., 1982. Calculation of multicomponent chemical equilibria and reaction processes in systems involving minerals, gases and an aqueous phase. Geochimica et Cosmochimica Acta 46, 513–528.

Rodríguez-Escales, P., Barba, C., Sanchez-Vila, X., Jacques, D., Folch, A., 2020. Coupling flow, heat, and reactive transport modeling to reproduce in situ redox potential evolution: Application to an infiltration pond. Environmental Science & Technology 54, 12092–12101.

Saaltink, M., Carrera, J., Ayora, C., 2000. A comparison of two approaches for reactive transport modelling. Journal of Geochemical Exploration 69, 97–101.

Saaltink, M.W., Carrera, J., Ayora, C., 2001. On the behavior of approaches to simulate reactive transport. Journal of Contaminant Hydrology 48, 213–235.

Sahimi, M., 2011. Flow and transport in porous media and fractured rock: from classical methods to modern approaches. John Wiley & Sons.

Samper, J., Juncosa, R., Delgado, J., Montenegro, L., 2000. Core^{2D}. A code for non-isothermal water flow and reactive solute transport. Users manual version 2. Technical Report. Empresa Nacional de Residuos Radiactivos.

Samper, J., Xu, T., Yang, C., 2009. A sequential partly iterative approach for multicomponent reactive transport with core^{2D}. Computational Geosciences 13, 301.

Scheidegger, A.E., 1961. General theory of dispersion in porous media. Journal of Geophysical Research 66, 3273–3278.

Seigneur, N., Vriens, B., Beckie, R., Mayer, K., 2020. Reactive transport modelling to investigate multi-scale waste rock weathering processes. Journal of Contaminant Hydrology 236, 103752.

Shao, H., Kosakowski, G., Berner, U., Kulik, D.A., Mäder, U., Kolditz, O., 2013. Reactive transport modeling of the clogging process at maqarin natural analogue site. Physics and Chemistry of the Earth, Parts A/B/C 64, 21–31.

Steefel, C.I., 2009. Crunchflow. Software for modeling multicomponent reactive flow and transport. User's manual. Lawrence Berkeley National Laboratory, Berkeley .

Steefel, C.I., 2019. Reactive transport at the crossroads. Reviews in Mineralogy and Geochemistry 85, 1–26.

Steefel, C.I., Appelo, C., Arora, B., Jacques, D., Kalbacher, T., Kolditz, O., Lagneau, V., Lichtner, P., Mayer, K., Meeussen, J., et al., 2015. Reactive transport codes for subsurface environmental simulation. Computational Geosciences 19, 445–478.

Steefel, C.I., DePaolo, D.J., Lichtner, P.C., 2005. Reactive transport modeling: An essential tool and a new research approach for the earth sciences. Earth and Planetary Science Letters 240, 539–558.

Steefel, C.I., Lasaga, A.C., 1994. A coupled model for transport of multiple chemical species and kinetic precipitation/dissolution reactions with application to reactive flow in single phase hydrothermal systems. American Journal of science 294, 529–592.

Steefel, C.I., Van Cappellen, P., 1990. A new kinetic approach to modeling water-rock interaction: The role of nucleation, precursors, and ostwald ripening. Geochimica et Cosmochimica Acta 54, 2657–2677.

Våg, J.E., Wang, H., Dahle, H.K., 1996. Eulerian-lagrangian localized adjoint methods for systems of nonlinear advective-diffusive-reactive transport equations. Advances in Water Resources 19, 297–315.

Valocchi, A.J., Malmstead, M., 1992. Accuracy of operator splitting for advection-dispersion-reaction problems. Water Resources Research 28, 1471–1476.

Van Genuchten, M.T., 1981. Analytical solutions for chemical transport with simultaneous adsorption, zero-order production and first-order decay. Journal of Hydrology 49, 213–233.

Walter, A., Frind, E., Blowes, D., Ptacek, C., Molson, J., 1994. Modeling of multicomponent reactive transport in groundwater: 2. Metal mobility in aquifers impacted by acidic mine tailings discharge. Water Resources Research 30, 3149–3158.

Wang, H., 1998. A family of ELLAM schemes for advection-diffusion-reaction equations and their convergence analyses. Numerical Methods for Partial Differential Equations: An International Journal 14, 739–780.

Wang, H., Ewing, R.E., Qin, G., Lyons, S.L., Al-Lawatia, M., Man, S., 1999. A family of Eulerian–Lagrangian localized adjoint methods for multi-dimensional advection-reaction equations. Journal of Computational Physics 152, 120–163.

Wang, X., Tchelepi, H.A., 2013. Trust-region based solver for nonlinear transport in heterogeneous porous media. Journal of Computational Physics 253, 114–137.

Wissmeier, L., Barry, D.A., 2011. Simulation tool for variably saturated flow with comprehensive geochemical reactions in two-and three-dimensional domains. Environmental Modelling & Software 26, 210–218.

Xu, T., Sonnenthal, E., Spycher, N., Pruess, K., 2006. Toughreact—a simulation program for non-isothermal multiphase reactive geochemical transport in variably saturated geologic media: applications to geothermal injectivity and co2 geological sequestration. Computers & Geosciences 32, 145–165.

Xu, T., Spycher, N., Sonnenthal, E., Zhang, G., Zheng, L., Pruess, K., 2011. Toughreact version 2.0: A simulator for subsurface reactive transport under non-isothermal multiphase flow conditions. Computers & Geosciences 37, 763–774.

Yapparova, A., Gabellone, T., Whitaker, F., Kulik, D.A., Matthäi, S.K., 2017. Reactive transport modelling of dolomitisation using the new CSMP++GEM coupled code: Governing equations, solution method and benchmarking results. Transport in Porous Media 117, 385–413.

Yapparova, A., Miron, G.D., Kulik, D.A., Kosakowski, G., Driesner, T., 2019. An advanced reactive transport simulation scheme for hydrothermal systems modelling. Geothermics 78, 138–153.

Yeh, G., Tripathi, V., 1989. A critical evaluation of recent developments in hydrogeochemical transport models of reactive multichemical components. Water Resources Research 25, 93–108.

Yuan, T., Ning, Y., Qin, G., 2016. Numerical modeling and simulation of coupled processes of mineral dissolution and fluid flow in fractured carbonate formations. Transport in Porous Media 114, 747–775.

Zienkiewicz, O.C., Taylor, R.L., Taylor, R.L., Taylor, R.L., 2000. The finite element method: solid mechanics. volume 2. Butterworth-heinemann.